THE CARNEGIE SUPERNOVA PROJECT: FIRST NEAR-INFRARED HUBBLE DIAGRAM TO $z \sim 0.7$[*]

WENDY L. FREEDMAN[1], CHRISTOPHER R. BURNS[1], M. M. PHILLIPS[2], PAMELA WYATT[1], S. E. PERSSON[1], BARRY F. MADORE[1],
CARLOS CONTRERAS[2], GASTON FOLATELLI[2,3], E. SERGIO GONZALEZ[2], MARIO HAMUY[3], ERIC HSIAO[4], DANIEL D. KELSON[1],
NIDIA MORRELL[2], D. C. MURPHY[1], MIGUEL ROTH[2], MAXIMILIAN STRITZINGER[2], LAURA STURCH[1], NICK B. SUNTZEFF[5],
P. ASTIER[6], C. BALLAND[6,7], BRUCE BASSETT[8], LUIS BOLDT[2], R. G. CARLBERG[9], ALEXANDER J. CONLEY[9],
JOSHUA A. FRIEMAN[10,11,12], PETER M. GARNAVICH[13], J. GUY[6], D. HARDIN[6], D. ANDREW HOWELL[14,15], RICHARD KESSLER[11,16],
HUBERT LAMPEITL[17], JOHN MARRINER[10], R. PAIN[6], KATHY PERRETT[9], N. REGNAULT[6], ADAM G. RIESS[18,19], MASAO SAKO[20],
DONALD P. SCHNEIDER[21], MARK SULLIVAN[22], AND MICHAEL WOOD-VASEY[23]
[1] Carnegie Observatories, 813 Santa Barbara Street, Pasadena, CA 91101, USA
[2] Carnegie Institution of Washington, Las Campanas Observatory, Colina El Pino, Casilla 601, Chile
[3] Universidad de Chile, Departmento de Astronomia, Casilla 36-D, Santiago, Chile
[4] Department of Physics and Astronomy, University of Victoria, P.O. Box 3055, Stn CSC, Victoria, BC V8W 3P6, Canada
[5] Physics Department, Texas A&M University, College Station, TX 77843, USA
[6] LPNHE, CNRS-IN2P3 and Universités Paris VI & VII, 4 place Jussieu, 75252 Paris Cedex 05, France
[7] APC, Collège de France, 11 place Marcellin Berthelot, 75005 Paris, France
[8] Department of Mathematics and Applied Mathematics, University of Cape Town, Rondebosch 7701, South Africa and South African Astronomical Observatory,
P.O. Box 9, Observatory 7935, South Africa
[9] Department of Astronomy, University of Toronto, 60 St. George Street, Toronto, ON M5S 3H8, Canada
[10] Center for Particle Astrophysics, Fermi National Accelerator Laboratory, P.O. Box 500, Batavia, IL 60510, USA
[11] Enrico Fermi Institute, University of Chicago, 5640 South Ellis Avenue, Chicago, IL 60637, USA
[12] Department of Astronomy and Astrophysics, The University of Chicago, 5640 South Ellis Avenue, Chicago, IL 60637, USA
[13] University of Notre Dame, 225 Nieuwland Science, Notre Dame, IN 46556-5670, USA
[14] Las Cumbres Observatory Global Telescope Network, 6740 Cortona Dr., Suite 102, Goleta, CA 93117, USA
[15] Department of Physics, University of California, Santa Barbara, Broida Hall, Mail Code 9530, Santa Barbara, CA 93106-9530, USA
[16] Kavli Institute for Cosmological Physics, The University of Chicago, 5640 South Ellis Avenue Chicago, IL 60637, USA
[17] Institute of Cosmology and Gravitation, University of Portsmouth, Portsmouth, P01 3FX, UK
[18] Department of Physics and Astronomy, Johns Hopkins University, Baltimore, MD 21218, USA
[19] Space Telescope Science Institute, 3700 San Martin Drive, Baltimore, MD 21218, USA
[20] Department of Physics and Astronomy, University of Pennsylvania, 209 South 33rd Street, Philadelphia, PA 19104, USA
[21] Department of Astronomy and Astrophysics, Pennsylvania State University, 525 Davey Laboratory, University Park, PA 16802, USA
[22] Department of Astrophysics, University of Oxford, Keble Road, Oxford OX1 3RH, UK
[23] Department of Physics and Astronomy, 3941 O'Hara Street, University of Pittsburgh, Pittsburgh, PA 15260, USA

ABSTRACT

The Carnegie Supernova Project (CSP) is designed to measure the luminosity distance for Type Ia supernovae (SNe Ia) as a function of redshift, and to set observational constraints on the dark energy contribution to the total energy content of the universe. The CSP differs from other projects to date in its goal of providing an *I*-band *rest-frame* Hubble diagram. Here, we present the first results from near-infrared observations obtained using the Magellan Baade telescope for SNe Ia with $0.1 < z < 0.7$. We combine these results with those from the low-redshift CSP at $z < 0.1$. In this paper, we describe the overall goals of this long-term program, the observing strategy, data reduction procedures, and treatment of systematic uncertainties. We present light curves and an *I*-band Hubble diagram for this first sample of 35 SNe Ia, and we compare these data to 21 new SNe Ia at low redshift. These data support the conclusion that the expansion of the universe is accelerating. When combined with independent results from baryon acoustic oscillations, these data yield $\Omega_m = 0.27 \pm 0.02(\text{statistical})$ and $\Omega_{\text{DE}} = 0.76 \pm 0.13(\text{statistical}) \pm 0.09(\text{systematic})$, for the matter and dark energy densities, respectively. If we parameterize the data in terms of an equation of state, w (with no time dependence), assume a flat geometry, and combine with baryon acoustic oscillations, we find that $w = -1.05 \pm 0.13(\text{statistical}) \pm 0.09(\text{systematic})$. The largest source of systematic uncertainty on w arises from uncertainties in the photometric calibration, signaling the importance of securing more accurate photometric calibrations for future supernova cosmology programs. Finally, we conclude that either the dust affecting the luminosities of SNe Ia has a different extinction law ($R_V = 1.8$) than that in the Milky Way (where $R_V = 3.1$), or that there is an additional intrinsic color term with luminosity for SNe Ia, independent of the decline rate. Understanding and disentangling these effects is critical for minimizing the systematic uncertainties in future SN Ia cosmology studies.

Key words: cosmology: observations – distance scale – supernovae: general

Online-only material: color figures

1. INTRODUCTION

Observations of high-redshift Type Ia supernovae (SNe Ia) currently provide the best evidence for an accelerating universe (Riess et al. 1998; Perlmutter et al. 1999; Knop et al. 2003;

Astier et al. 2006; Wood-Vasey et al. 2007; Hicken et al. 2009). Independently, the *Wilkinson Microwave Anisotropy Probe* (*WMAP*) measurements of fluctuations in the cosmic microwave background (CMB; Spergel et al. 2003, 2007); detections of acoustic oscillations in the matter density spectrum (Eisenstein et al. 2005); as well as the comparison of Hubble expansion ages from the Hubble Key Project (Freedman et al. 2001) with the ages of Milky Way globular clusters (Krauss & Chaboyer 2003), have all led to the growing body of evidence for a dark-energy component to the overall mass–energy density of the universe (see also Frieman et al. 2008 for a recent review). The above studies yield results consistent with a flat universe where the sum of the dark energy and matter densities $\Omega_{DE} + \Omega_m = 1$, and where $\Omega_{DE} \sim 0.7$, with a matter density $\Omega_m \sim 0.3$.

At present, a physical understanding of this dark-energy component remains elusive, and there is a wide variety of possible alternatives ranging from the cosmological constant, as originally proposed by Einstein in 1917; a decaying scalar field; or perhaps even a modification of general relativity. A convenient measure is w, the ratio of pressure P to energy density ρ, where $w = P/\rho$. In the case of a cosmological constant, $w = -1$. The time evolution of w is not known at present. Given our currently limited understanding of this critical component of the universe, it is clear that further observational and experimental data are needed to constrain and characterize the properties of dark energy.

SNe Ia show a relation between peak brightness and rate of decline, in addition to color (or reddening). Accounting for these correlations yields a dispersion in the Hubble diagram of about 7% in distance (Phillips 1993; Hamuy et al. 1995; Riess et al. 1996; Hamuy et al. 1996a; Astier et al. 2006). As more and more SNe Ia are discovered and the statistical uncertainties in this method are decreased, the challenge becomes understanding and controlling the remaining systematic uncertainties, as well as testing for currently unknown systematic effects. A well-known systematic is reddening and extinction due to dust, and there may potentially be differences due to chemical composition and age of the progenitors or their environment. The requirement for increasing measurement accuracy, the lack of a detailed theoretical understanding of SN Ia, the fact that most observations have been made at rest-frame optical and ultraviolet colors (where reddening uncertainties are large), the difficulty of obtaining accurate K- and spectral corrections, all point to the need to characterize and decrease these systematic errors and uncertainties. As other errors have been reduced over time, those which were relatively small effects previously, have now become increasingly important as the required precision in cosmology has risen.

Observations of SNe Ia at near-infrared (NIR) wavelengths offer several advantages in minimizing a number of systematic effects (most notably reddening), as well as providing an additional, independent probe of the expansion history. We make use of the Y band, centered near 1.035 μm (Hillenbrand et al. 2002), which falls in between the traditionally classified optical and infrared spectral regimes. The Y and J (1.25 μm) bands provide a means of obtaining *rest-frame I*-band magnitudes for SNe Ia in the redshift range 0.1–0.7, an interval covering the time at which the influence of dark energy begins to dominate the expansion. Hence, NIR observations offer an important opportunity both to minimize systematic uncertainties and yield an independent Hubble diagram.

Aside from a few observations published by Riess et al. (2000) and Nobili et al. (2005), rest-frame *I*-band measurements have not yet been routinely undertaken at higher redshifts because at $z \sim 0.25$ the *I*-band is redshifted beyond the CCD sensitivity limit at red wavelengths. A further challenge to NIR photometry obtained from the ground is that the sky background is much greater than at optical wavelengths. As a consequence, observing distant SNe Ia in the NIR is expensive in telescope time. However, since current searches to find SNe Ia now yield extensive optical coverage of the light curves, the decline rates and time of maximum light are already well defined, so that fewer observations are required to derive NIR light-curve parameters accurately. With the availability of 6.5 meter class telescopes and NIR arrays, a NIR study of SNe Ia at $z > 0.1$ has now become feasible.

Ongoing optical surveys aimed at discovering large samples of SNe Ia are significantly decreasing the statistical uncertainties in SN Ia cosmology measurements, while simultaneously aiming to reduce the systematic errors. The Carnegie Supernova Project (CSP) is complementary to these studies; that is, it is not designed to rival optical surveys on numbers of objects and statistical errors, but rather it is more focused on follow-up observations critical to testing for and minimizing systematic uncertainties. These follow-up observations (multiple wavelengths at low redshift and NIR observations at higher redshifts) require more observing time per individual SN Ia. An understanding of the systematic errors is a critical goal for all SN Ia programs.

To date, as part of the high-redshift CSP, we have obtained NIR observations of 80 SNe Ia. Subsequent host-galaxy observations have been obtained for 71 objects; and we have fully analyzed 35 objects, the sample for which photometry, light curves, and a preliminary Hubble diagram are presented in this paper.

2. THE CARNEGIE SUPERNOVA PROJECT

The CSP is an umbrella name for our two coordinated SN programs: one being carried out at the Las Campanas 1 m Swope and 2.5 m Dupont telescopes for low ($0 < z < 0.1$) redshift objects, and the other using the Magellan Baade 6.5 m telescope at higher ($0.1 < z < 0.7$) redshifts. Preliminary results from the low-redshift part of this project have been reported in Hamuy et al. (2006), Folatelli et al. (2006), and Phillips et al. (2007); the most recent results are presented in two companion papers (Contreras et al. 2009; Folatelli et al. 2009). The CSP is not a SN *search* program; rather as described below, as well as in Hamuy et al. (2006), we are using the facilities of the Las Campanas Observatory, in coordination with several ongoing search programs elsewhere, to provide detailed and immediate *follow-up* observations of newly discovered SNe.

2.1. Goals

Overall, the CSP is focused on obtaining observations of SNe Ia falling in the redshift range $0 < z < 0.7$. As described in Hamuy et al. (2006), at low redshifts we are currently obtaining 10-filter ($uBVgriY JHK_s$) photometry with excellent time sampling and optical spectroscopy to provide a database for the determination of the Hubble constant, accurate K-corrections, comparison with theoretical models of SNe Ia, and a fundamental data set for comparison with high redshift. At high redshifts, as described in this current paper, we are obtaining YJ data near maximum light. The NIR data, in conjunction with optical photometry (being obtained as part of the search programs), allow the determination of reddening

Table 1
Filter Nomenclature

| Name	Average Wavelength (Å)	Description	Zero Point	Reference
Y	10333.6	Y-band on PANIC, Magellan I, LCO	12.6870	Persson et al. (1998)
J	12440.3	J-band on PANIC, Magellan I, LCO	12.8520	"
B	4414.0	B-band on Swope, LCO	13.6672	Hamuy et al. (2006)
V	5408.6	V-band on Swope, LCO	13.7758	"
i	7609.2	i-band on Swope, LCO	13.6873	"
g_m	4905.0	g-band on Megacam, CFHT	15.5363	Astier et al. (2006)
r_m	6282.6	r-band on Megacam, CFHT	14.8061	"
i_m	7725.0	i-band on Megacam, CFHT	14.5543	"
z_m	8901.6	z-band on Megacam, CFHT	13.9996	"
g_s	4718.9	g-band on 2.5m, APO	14.2013	Smith et al. (2002)
r_s	6185.2	r-band on 2.5m, APO	14.2157	"
i_s	7499.7	i-band on 2.5m, APO	13.7775	"
R_{4m}	6660.2	R-band on 4m Blanco telescope, CTIO	15.1820	Miknaitis et al. (2007)
I_{4m}	7973.8	I-band on 4m Blanco telescope, CTIO	14.4580	"

corrections and a rest-frame I-band Hubble diagram. One of the key goals of the CSP is to minimize the effects of reddening in the Hubble diagram, and ensure that the *rest-frame* (BVi) bandpasses, being observed at low redshift, match those for a sample at higher redshift, so that reddening corrections can be applied in a uniform way. Ultimately, the goal is to measure accurate luminosity distances to better constrain cosmological models. Assuming a model including dark energy, the goal is to characterize the acceleration of the universe and constrain the equation of state, w, to a precision *and accuracy* of $\pm10\%$.

2.2. "I-band" Filter Nomenclature

There are many "I-band" filters in current use. We distinguish here between the Kron-Cousins I-band, the SNLS MegaCam i_M band (based on Landolt standards calibrated to Vega), and the SDSS-II i_S band (based on a calibration tied to four subdwarfs, Smith et al. 2002). Our Las Campanas natural i-band calibration is also tied to Smith et al. The central wavelengths of these (and other) passbands are defined in Table 1. In this paper, we also refer to a generic "I band" when collectively speaking about observations in the NIR wavelength range $\sim 8000\,\text{Å}$.

2.3. I-band Light Curves SNe Ia

The form of NIR light curves for SNe Ia differs from those at optical wavelengths. At *IYJH* and *K*, the light curves show a minimum following maximum light, followed by an additional secondary maximum, less luminous than the primary peak (e.g., Elias et al. 1985; Hamuy et al. 1996c; Meikle 2000; Krisciunas et al. 2001; Nobili et al. 2005). This secondary maximum is thought to be the result of a sudden drop in the mean opacity in the SN ejecta (Pinto & Eastman 2000; Kasen 2006). In Figure 1, we show some examples of i-band light curves for four well observed, nearby SNe Ia from the low-z CSP sample. Our strategy for the high-redshift CSP is to obtain i photometry covering the first peak only, and to avoid the (fainter) secondary maximum. The optical surveys already provide measurements of the decline rate in the B band, so duplication of these data is not required. The median start and end times of our observations are 0 and +12 days with respect to observed i-band maximum, respectively. In this paper, unless otherwise noted, we refer to the observed (not rest) frame time.
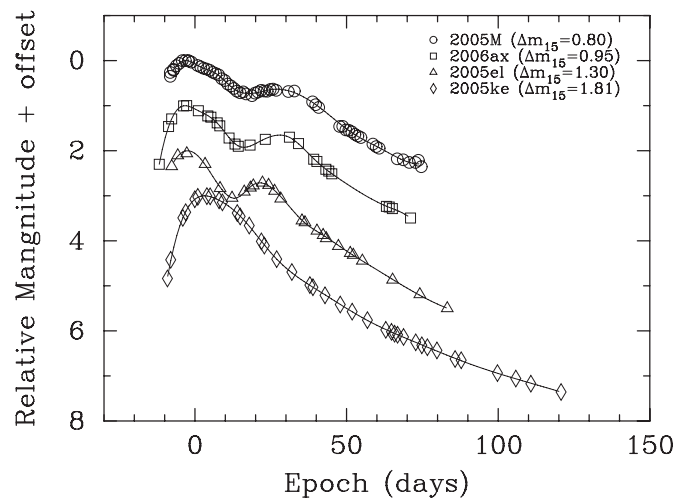
Figure 1. Representative sample of four i-band light curves from the low-z CSP sample chosen to illustrate the behavior of the secondary maximum. For clarity, the light curves have been normalized to their peak magnitudes and then offset by one magnitude from each another. The SNe Ia have values of Δm_{15} ranging from 1.12 to 1.81. The fast-declining SN Ia with $\Delta m_{15} = 1.81$ (bottom light curve) shows no secondary maximum.

2.4. Targets

There have been four ongoing SN search programs with which the CSP has been actively collaborating. At low redshifts ($z < 0.1$), we are collaborating with the Lick Observatory Supernova Search (LOSS), as described in Hamuy et al. (2006). For intermediate redshifts ($0.1 < z < 0.4$), we have been collaborating with the Sloan Digital Sky Survey II (SDSSII), while the CFHT Legacy Survey (SNLS) and ESSENCE found SNe Ia out to higher redshifts ($0.1 < z < 0.7$). The three surveys relevant to this higher redshift study are described briefly below.

2.4.1. Sloan Digital Sky Survey (SDSS) II

An extension to the Sloan Digital Sky Survey (York et al. 2000), the SDSS-II,[24] (Sako et al. 2008; Frieman et al. 2008) has completed a three-year rolling search program using the 2.5 m SDSS telescope to discover intermediate redshift ($0.05 < z < 0.35$) SNe Ia in a 300 deg^2 southern equatorial field,

---

[24] http://www.sdss.org

obtaining multicolor (*ugriz*) photometry with a cadence of $\sim$2–5 days. The data were obtained during the months of September through 2005–2007 November. Spectra to determine redshifts and types for the SDSSII candidates were obtained with several telescopes with a range of apertures. Photometry for the 130 spectroscopically confirmed SNe Ia from the 2005 season have been presented in Holtzman et al. (2008).

2.4.2. CFHT Legacy Survey (SNLS)

The Supernova Legacy Survey,[25] a Canadian/French collaboration, used the CFHT and the 1 deg^2 camera (MegaCam) to obtain deep optical ($u'g'r'i'z'$) images for four fields, each of approximately 1 deg^2 around the equator (Astier et al. 2006), beginning in 2003 February. The SNLS was also a rolling search program in which each field was revisited every second night during a five month campaign each semester for a total of five years. Spectroscopic follow-up for the SNLS candidates was obtained at the 10 m Keck telescope, the 8 m Very Large Telescope (VLT), the 8 m Gemini North and South telescopes, as well as the Magellan telescopes. In their first year of operation, they discovered 91 SNe Ia, and published data for a sample of 71 SNe Ia with redshifts $0.1 < z < 1.1$. In total, about 450 SNe Ia have been discovered.

2.4.3. ESSENCE

ESSENCE[26] completed its survey using the 4 m CTIO Blanco telescope and MOSAIC II wide-field camera covering equatorial fields at *VRI* wavelengths over the redshift range between $0.15 < z < 0.75$ (Matheson et al. 2005; Miknaitis et al. 2007). The goal was to provide optical light curves for about 200 Type Ia SNe Ia over five years (2002–2007). ESSENCE was scheduled for 30 half nights during a three month (October–December) campaign each year. The observing was centered on new moon, and was scheduled every other night, for a span of 20 days, with a gap of 10 bright nights per month. Spectroscopic follow-up for the ESSENCE candidates was obtained at Gemini North and South, Keck, the VLT, MMT, and Magellan telescopes. At the time of writing, ESSENCE has published observations for 102 SNe Ia (Wood-Vasey et al. 2007).

2.5. CSP Magellan Follow-up Observations

Our follow-up Magellan observations consist of *Y*- and/or *J*-band images. We chose not to observe at *H* band because of the increased sky background produced by atmospheric OH airglow emission. Optical photometry for this sample of SNe Ia was obtained during the course of the original surveys (SDSS-II, ESSENCE, and SNLS), and was not repeated. The Sloan *i* filter, which we are using at the Swope telescope for the low redshift part of the CSP, overlaps well with the *Y* band for a redshift of $z \sim 0.35$, and the *J* band at redshift $z \sim 0.63$ (see Figure 2). If targets at these redshifts were available, they moved to the top of our observing priority list. We aimed to obtain Magellan observations no more than a few days after maximum light, and preferably while still on the rise. Our criteria for selection of the SNLS, ESSENCE, and SDSS-II objects were: (1) the SNe Ia were in the redshift range $0.2 < z < 0.7$, (2) the SN Ia was estimated to be near maximum, (3) SNe Ia near $z = 0.35$ and $z = 0.65$ were given preference, and (4) preference was given to SNe Ia well-separated from the host. In practice, criteria (3) and
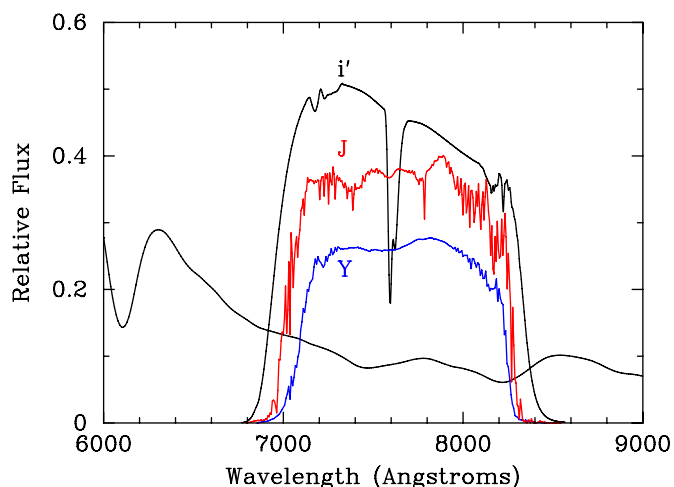
Figure 2. Filter response functions for the *Y* (blue) and *J* (red) bands blueshifted by 0.35 and 0.63, respectively. Rest-frame *i* band is plotted in black. The absorption feature at $\lambda \sim 7600\,\text{Å}$ is telluric O_2. Crossing the entire figure, the SED of a typical SN Ia at maximum (Hsiao et al. 2007) is also shown in black.
(A color version of this figure is available in the online journal.)

(4) were rarely invoked since there was not much choice after criteria (1) and (2). Our selection criteria, therefore, matched fairly closely those of the parent surveys.

The SNLS, ESSENCE, and SDSS-II projects provided coordinates, finder charts and epochs of high-probability SN Ia candidates for the Magellan observations. In three cases (SNLS 03D1gl, SNLS 04D2cw, and ESSENCE 2004-H-280), the spectral classifications were later revised (to types other than SNe Ia). In one case (SNLS 04D2al), the redshift was too large ($z = 0.838$) and the SN Ia was undetectable in our observations. In Table 2, we list the SN Ia name, position, number of CSP observations, and IAU cross identification, for the SNe Ia.

3. INSTRUMENTATION AND OBSERVATIONS

3.1. Instrumentation

Our NIR imaging has been carried out using *Y*- and *J*-band filters on the Persson Auxiliary Nasmyth Infrared Camera (PANIC; Martini et al. 2004). This camera is mounted on the east Nasmyth platform of the Magellan Baade telescope. It contains a 1024×1024 HgCdTe Hawaii-1 array with a scale of 0.125 arcsec pixel^{-1}, and covers a field of view of $2\farcm1 \times 2\farcm1$ on the sky.

3.2. Observations

3.2.1. Observing Strategy and Current Status

Our observing goal was to acquire *Y* and/or *J* photometry with gaps in the SN Ia light curves no larger than 7 days, straddling the light curve over maximum light if possible. To avoid large gaps, PANIC was scheduled during dark/gray time, in addition to the customary bright time for infrared instruments. In practice, telescope time was scheduled with gaps generally less than 5 days, although gaps of 8 days were occasionally unavoidable. A record of observations, including finding charts of the objects, is maintained on our Web site for the project, which can be found at http://www.carnegiescience.edu. Generally, 3 to 5 observations per SN Ia were obtained.

We began this long-term project with a pilot program in 2003 November running through 2004 April, centered on the best

Table 2
CSP High-z SNe

Name	R.A. (2000) (h:m:s)	Decl. (2000) ($°:':''$)	Epochs	z	Cross ID
SNLS 03D4gl	22:14:44.16	−17:31:44.40	3	0.571	...
SNLS 04D1oh	02:25:02.38	−04:14:10.68	2	0.59	...
SNLS 04D1pg	02:27:04.15	−04:10:31.33	3	0.515	...
SNLS 04D1rh	02:27:47.16	−04:15:13.68	4	0.435	...
SNLS 04D1sk	02:24:22.56	−04:21:13.32	2	0.6634	...
SNLS 04D2an	10:00:52.32	02:02:28.68	8	0.62	...
SNLS 05D1dn	02:24:26.64	−04:59:29.40	4	0.566	...
SNLS 05D1hk	02:24:39.17	−04:38:03.01	2	0.2631	...
SNLS 05D1hn	02:24:36.26	−04:10:54.95	1	0.1489	...
SNLS 05D1ix	02:24:19.94	−04:40:11.75	3	0.49	...
SNLS 05D1iy	02:27:39.96	−04:25:21.36	1	0.2478	...
SNLS 05D2ah	10:01:28.80	01:51:46.08	6	0.184	...
SNLS 05D2bt	10:01:40.32	02:33:57.96	5	0.679	...
SNLS 05D2bv	10:02:17.04	02:14:26.16	5	0.474	...
SNLS 05D2ck	10:00:45.12	02:34:22.08	4	0.698	...
SNLS 05D2dw	09:58:32.16	02:01:56.28	2	0.417	...
SNLS 05D2eb	10:00:14.64	02:24:26.64	2	0.5344	...
SNLS 05D2mp	09:59:08.64	02:12:14.69	3	0.3537	...
SNLS 05D4cw	22:14:50.16	−17:44:19.32	3	0.375	...
SNLS 05D4fo	22:15:20.88	−17:16:05.16	4	0.373	...
ESS d149wcc4-11	02:10:53.98	−04:25:49.80	3	0.342	SN2003jy
ESS e108wdd8-4	02:30:09.00	−09:04:35.76	3	0.469	SN2003km
SDSS 12855	22:01:01.44	00:42:58.47	2	0.165	...
SDSS 13025	22:46:16.08	00:24:57.21	3	0.224	...
SDSS 13835	00:24:14.31	−00:14:53.69	2	0.247	...
SDSS 15287	21:35:50.40	−01:03:26.75	1	0.235	...
SDSS 16442	21:59:47.28	−00:43:59.59	3	0.281	...
SDSS 3241	20:50:36.24	−00:21:14.76	5	0.259	SN2005gh
SDSS 3331	02:18:14.74	00:47:47.76	5	0.208	SN2005ge
SDSS 4679	01:26:06.79	00:40:36.80	4	0.333	SN2205gy
SDSS 5183	03:33:48.96	00:42:33.70	6	0.384	SN2005gq
SDSS 5549	00:13:00.13	00:14:53.70	5	0.119	SN2005hx
SDSS 6699	21:31:15.60	−01:03:25.16	4	0.311	SN2005ik
SDSS 7243	21:52:18.96	00:28:19.09	3	0.204	SN2005jm
SDSS 7512	03:28:21.67	−00:19:34.10	2	0.22	SN2005jo

weather period at Las Campanas. Our first host-galaxy images (once the SN Ia had faded) were obtained in the following year. In the second year, we observed from 2004 October through 2005 March. Unfortunately, poor weather at Mauna Kea during the northern winters of 2003 and 2004 resulted in a very low yield of SNe Ia for CSP follow-up during this pilot project. Moreover, ESSENCE was operational only during the northern fall, and SDSS-II began routine operations during the fall of 2005. We, therefore, shifted the CSP follow-up campaigns to August through January when there was good overlap with all three SN search programs.

After four campaigns, we obtained Y and/or J photometry for a total of 80 objects, 75 of which were ultimately confirmed as SNe Ia. Follow-up host-galaxy observations have been obtained for 71 of these SNe Ia, and we are in the process of obtaining host-galaxy images for the remaining objects. The redshift distribution for our total sample is shown in Figure 3. In this paper, we report on the photometry from the first 35 SNe Ia. A summary of the observations for these 35 SNe Ia is given in Table 2. At the current time, data for 20, 13, and 2 SNe Ia have been analyzed from the SNLS, SDSS-II, and ESSENCE surveys, respectively. The original goal of the CSP was to acquire a sample of 100 objects over the redshift range $0.1 < z < 0.7$; however, with the conclusion of the three surveys, our expected sample will be limited to 75 SNe Ia.
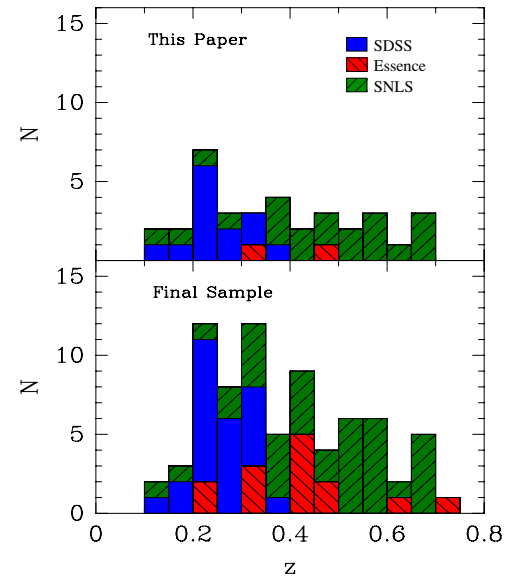
Figure 3. Redshift distribution of objects observed as a part of the CSP in the NIR on Magellan. In general, the higher redshift objects are found by the SNLS, and those at lower redshifts primarily by the SDSS-II. We have observed 14 objects discovered by ESSENCE, 37 SNLS objects, and 24 SDSS objects.

(A color version of this figure is available in the online journal.)

3.2.2. Observing Procedures

Twilight sky flats were taken in each filter every night in at least five dithered positions with 2 exposures at each position, controlling the count level to be in the linear regime. The detector becomes nonlinear at the 1% level at approximately 13,000 ADU and at the 5% level at approximately 35,000 ADU. Dark frames were taken in sets of 15, each with exposure times matching those of the science images. The SN Ia observations were obtained using nine dither positions with two exposures per position. The exposure times used for individual images were 120 s with total exposure times ranging from 2160 to 8640 s. Reference images for these SN Ia fields were taken in the same manner once the SN Ia faded, to allow accurate background subtraction. The signal to noise in the stacked reference images were as high (or higher) than those in the SN Ia images, so as not to degrade the photometry. The seeing for these images ranged typically between 0.4 and 0.8 arcsec. On photometric nights, three to five stars chosen from the standard system defined by Persson et al. (1998) were observed throughout the night in each filter. These standard stars were observed in five dither positions with two exposures at each position. The exposure times of individual images were 3 or 4 s, resulting in total exposure times of 30 and 40 s. On occasion, the telescope was defocused to ensure the counts remained in the linear regime of the detector.

4. DATA ANALYSIS

4.1. Pipeline Processing

We have developed an automated pipeline to process the PANIC images. The pipeline carries out (1) linearity corrections, (2) dark combination and subtraction, (3) bad pixel mask production, (4) flat-field combination and division, (5) sky image computation and subtraction, and (6) combination of dithered frames into final stacked images. We apply a predetermined linearity correction law to every pixel value above 8000 ADU. The multiplicative correction ranges from 1.0 at 8000 ADU to 1.06

at 40,000 ADU. Dome flats are created by subtracting images of equal exposure times taken with no dome lamps from those with the dome lamps on. The final dome flats are used only to build bad pixel masks for each night and median-combined twilight sky flats are used for flat fielding. Sky frames are subtracted from the individual object frames using modal scale factors. Finally, stacked images are created by aligning and averaging the individual object frames.

4.2. Galaxy Template Subtraction

To obtain accurate photometry for the SNe Ia, the host-galaxy light must be subtracted from the images. The strategy for removing the host galaxies from the SN Ia data involves three steps: (1) obtaining host-galaxy images of the SN Ia fields in the year following the events; (2) registering and matching the point-spread functions (PSF) of the images; and (3) subtracting the PSF-matched SN Ia and host-galaxy images. The algorithm developed for the registration and nonparametric matching of the PSFs will be described in more detail in a later paper (D. Kelson et al. 2010, in preparation); the method is summarized briefly here.

For a given SN Ia image and associated host-galaxy image, SExtractor (Bertin & Arnouts 1996) is used to identify objects down to a threshold of 3σ. The positions of these objects are used to compute the coordinate transformation between each SN Ia image and the host-galaxy image. Matching the PSF of the host-galaxy image, T, to that of the SN Ia image, S, consists of solving for the convolution kernel, k, that maps point sources in T to S. Once k is known, the entire host-galaxy image can then be convolved with k and subtracted from S to isolate the SN Ia. However, our fields of view are small and in several instances lack suitable point sources for determining the kernel using more traditional techniques, for example, parameterizing the kernel with a Gaussian (Alard & Lupton 1998; Alard 2000). Instead, we use a nonparametric technique that utilizes all objects in the field to constrain the kernel. The kernel consists of a $(2M + 1) \times (2M + 1)$ matrix indexed by u and v, and is determined by minimizing

$$\chi^2 = \sum_i^N \left| \frac{S(x_i, y_i) - \sum_u \sum_v k(u, v) [T(x_i - u, y_i - v)]}{\sigma(x_i, y_i)} \right|^2,$$
(1)

where the sum is over N pixels in the source and template images.

The matrix of $T(x_i - u, y_i - v)$ is decomposed using singular value decomposition, and its constituent eigenvectors contain the kernel's natural set of orthogonal basis functions. The eigenvalues represent each eigenvector's sensitivity to noise. We eliminate those basis functions that do not contribute to reducing the χ^2 per degree of freedom. Because image rebinning is mathematically equivalent to a convolution, errors in the registration are fully accounted for by the convolution kernel that minimizes χ^2.

Ideally, one wishes to convolve (i.e., degrade) the host-galaxy images so as not to decrease the signal to noise of the SN Ia. However, approximately 8% of our SN Ia images were taken under exceptional seeing conditions (less than 0.35 arcsec) which, to date, have not been matched in our host-galaxy observations. As a result, this subset of the SN Ia images have to be degraded to match the poorer image quality of the host-galaxy images. Fortunately, these SNe Ia have lower redshifts ($z \leqslant 0.3$) and are relatively bright, so that the signal to noise
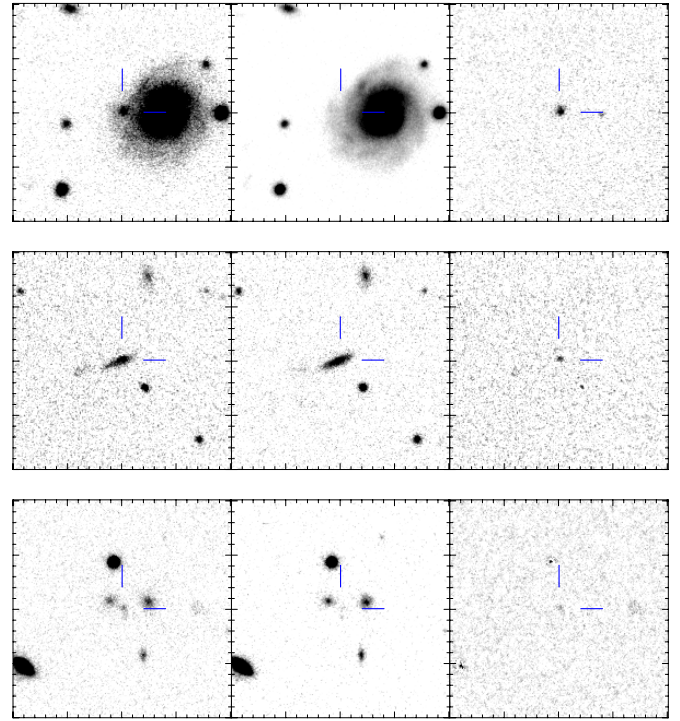
Figure 4. Sample of SNe Ia, post-SNe Ia and difference frames for three SNe Ia: SN 3241 (discovered by SDSS-II, top panel), 04D1rh (discovered by SNLS, middle panel), and 05D2bt (discovered by SNLS, bottom panel). SN 3241 ($z = 0.25$) was observed in the Y band, 04D1rh ($z = 0.435$) was observed in both Y and J (J is shown), and 05D2bt ($z = 0.679$) was observed in the J band. The scale of these images is 200 pixels = 25 arcsec on a side.

(A color version of this figure is available in the online journal.)

remains high. The SN Ia images in our sample to date have a range of image quality, from 0.3 arcsec to 1.4 arcsec; the host-galaxy images have a range of image quality, from 0.3 arcsec to 1.3 arcsec. We find that our image subtraction technique works well for removing the host galaxies for a wide range of seeing conditions, position of the SN Ia relative to the host galaxy, and redshift. Three examples of a host-galaxy-subtracted image are shown in Figure 4, for objects at redshifts of 0.25, 0.30, and 0.68, respectively.

4.3. Photometry

Observing SNe Ia in the NIR is more challenging than in the optical owing to higher sky background. The contrast of SN Ia to galaxy is also less in the red, and overcoming these effects require longer integrations than in the optical. We measure the flux with a two-step approach. The first step is to measure the magnitudes of several stars in each SN Ia field, which we shall refer to as tertiary standards. The primary standards are those that establish the JHK system (Elias et al. 1982), on which the secondary standards (Persson et al. 1998) that we observe are based. In choosing the tertiary standards, we require that: (1) the star is no closer than 20 arcsec to the edge of the PANIC field of view; (2) the star appears in all observations of the SN Ia and the host galaxy; and (3) there are no significant residuals for the star after host-galaxy subtraction. We use DAOPHOT and DAOGROW (Stetson 1990) to measure and fit a growth curve (flux versus aperture size) for each star. We then compute an aperture correction using these fits to get the flux measured through a 10-arcsec-diameter aperture, matching the aperture used on the standards. These fluxes are therefore calibrated with

respect to the secondary standards observed that evening, and are then averaged over all photometric nights.

The second step is to measure the flux ratios between the SN Ia and the tertiary standards. At the highest redshifts, we are working at the detection limit of the telescope where DAOPHOT and DAOGROW are no longer robust. Instead, we use the optimized extraction algorithm of Naylor (1996). In brief, the brighter stars in the field are used to estimate the PSF, $P_{i,j}$, modeled as a superposition of Gaussian and Moffat profiles. This estimated PSF is then used as a weight mask in summing the flux from the SN Ia pixels: $F = \sum_{i,j} w_{i,j}(D_{i,j} - S_{i,j})$ where $w_{i,j} = \frac{P_{i,j}}{\sum P_{i,j}^2}$, P is the model PSF, D is the measured counts, and S is the sky flux. Following Naylor (1996), we have assumed that the variance in the weights is dominated by the sky ($V_{ij} \simeq V_s$ in his Equation (10)). This yields an optimized estimate of the flux for the SN Ia. We then use the same weight mask to measure fluxes and compute flux ratios between the SN Ia and each tertiary standard. These flux ratios, together with the calibrated fluxes from step 1, provide estimates of the calibrated flux of the SN Ia. These estimates are averaged to yield the final calibrated flux for the SN Ia. We have done a number of tests in which fake point sources are inserted into the frames and then recovered, and find that the method works extremely well. These results will be reported in D. Kelson et al. (2010, in preparation).

We have also taken great care in computing the variances of our fluxes. In the process of correcting for image distortion in the PANIC pipeline, rectifying the images, convolving with a kernel, and then subtracting a host galaxy image, the pixels in each image have become correlated. We produce variance maps for each observed field early in the PANIC pipeline. A simple propagation of errors is done at each step of the pipeline, updating the variance in each pixel in the maps. The final variance maps are used to compute the noise rather than image statistics, ensuring that we can properly estimate the variance of the tertiary standards and the SN Ia.

4.4. Absolute Calibration

The absolute calibration of the Magellan photometry is based on *JHK* standard stars from Persson et al. (1998), where the zero point is tied to Vega. Currently, we are applying the *Y*-band absolute calibration described in Hamuy et al. (2006), using Kurucz model spectra and Hillenbrand et al. (2002) standard star measurements. Contreras et al. (2009) have recently obtained new observations confirming this calibration to an accuracy of ±0.01 mag. We have observed common standard stars and adopted the same procedures for the reduction of the standard stars so that differences in the calibration of low- and high-*z* samples are minimized. Adopting atmospheric extinction coefficients of $k_Y = 0.10$ and $k_J = 0.12$ mag/airmass following Hamuy et al., we solve for the nightly zero points in each filter. Photometry for the standard stars is obtained with apertures of diameter 10 arcsec. The statistical errors in the zero point are determined from the scatter of individual measurements and range from ± 0.01 to ± 0.05 mag. A minimum of three photometric nights determines the absolute flux for each SN Ia (see Section 4.3). The average scatter in the zero points based on observations of standard stars is 0.023 mag at *J* and 0.013 mag at *Y*.

In this (and other CSP) papers, we are presenting our photometry in our own natural system. The advantage of using the natural system is that it avoids the uncertainties resulting from

the broad features present in the spectra of SNe Ia, which present challenges for the transformation onto the standard system. As outlined in Contreras et al. (2009), the natural photometry is obtained by first computing color terms that transform local standard sequences of stars to the system appropriate for each filter (Landolt 1992 standards for *BV*, Smith et al. 2002 standards for *ugri*, and Persson et al. 1998 for *YJ*). These color terms are then used in reverse to transform the standard magnitudes to our natural system and it is these magnitudes that are used to calibrate the SN Ia photometry. The natural magnitudes are therefore equal to the standard magnitudes at zero color. Our natural system magnitudes can be straightforwardly transformed to other systems. Transmission curves for our NIR and optical filters are given in Hamuy et al. (2006) and Contreras et al. (2009), and updated versions are available online at the CSP Web site. In the SN Ia target fields, we identified several isolated stars to serve as tertiary standards to determine absolute flux for those nights that were not photometric. Photometry for these secondary standards is also available online. In Table 1, we list the filters, effective wavelengths, and published references to the calibrations relevant for the CSP. A comparison of our own NIR *YJ* photometry (*K*-corrected to the *i* band) to that of the optical surveys (SNLS, ESSENCE, and SDSS-II) requires that we adopt a standard with a measured spectral energy distribution (SED) spanning the optical and NIR. For this purpose, we have chosen the Bohlin & Gilliland (2004) model for Vega, as updated in Bohlin (2007).

5. SYSTEMATIC EFFECTS

As the number of objects has increased, SN Ia cosmology has reached the stage where the systematic uncertainties are becoming the dominant source of error. The CSP has been designed to minimize known systematic effects, particularly those due to *K*-corrections, reddening, and cross calibrations to different photometric systems. Below we discuss our current approach to deal with *K*-corrections and reddening.
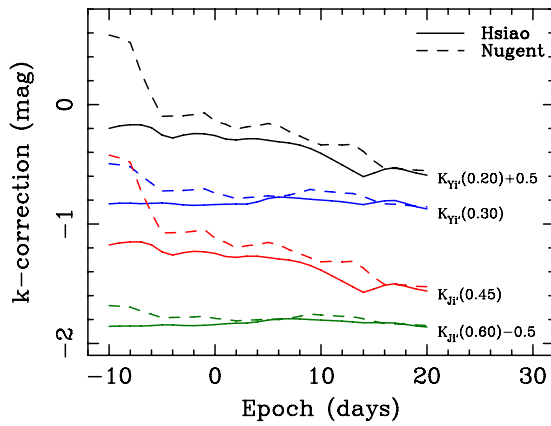
5.1. K-corrections

The observed SEDs of SNe Ia are shifted and stretched with redshift due to the expansion of the universe. Accurate corrections for these effects (*K*-corrections) for SNe Ia remain an observational challenge, and much effort has been put into creating libraries of SN Ia spectra with which to assemble SEDs that can be used to estimate the *K*-corrections and their variance (Nugent et al. 2002; Hsiao et al. 2007). The *K*-corrections are computed in a manner similar to Kim et al. (1996) and Nugent et al. (2002), using the following formula:

$$K_{AB}(t) = 2.5 \log(1+z)$$
$$+ 2.5 \log \left[\frac{\int R_B(\lambda) \Phi'(\lambda; t) \lambda d\lambda}{\int R_A(\lambda) \Phi'(\lambda(1+z); t) \lambda d\lambda} \right] + \mathcal{Z}_A - \mathcal{Z}_B,$$

(2)

where *A* represents the observed filter and *B* represents the rest-frame filter to which we are transforming, R_A and R_B are the corresponding observed and rest-frame filter response curves, and $\mathcal{Z}_A$ and $\mathcal{Z}_B$ are the photometric zero points. The *K*-corrections are therefore applied in the following sense: $m_B = m_A - K_{AB}$. The SED $\Phi'(\lambda; t)$ at epoch *t* is obtained by "color-matching" the corresponding SED template from Hsiao et al. (2007). Initially, *K*-corrections are computed using unmodified Hsiao et al. (2007) SED templates and applied to the
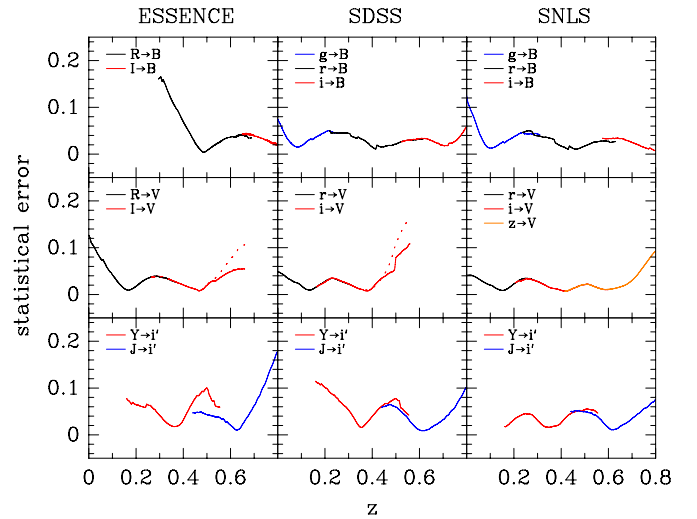
Figure 5. Crossband K-corrections (K_{iJ} and K_{iY}), based on SED templates of Hsiao et al. (2007) and Nugent et al. (2002), shown as a function of epoch for redshifts $z = 0.20$, 0.30, 0.45, and 0.60. The solid lines are the Hsiao et al. corrections and the dashed lines are Nugent et al. The largest differences occur at about 10 days before maximum. Given the significantly larger template library available to Hsiao et al., and the corrections for the telluric features, we have adopted the Hsiao et al. corrections.

(A color version of this figure is available in the online journal.)

Figure 6. Estimated dispersion in the K-corrections as a function of redshift for different photometric filter sets. Solid lines represent the dispersion when full optical and NIR filter sets are used to color-correct the template SED, whereas dashed lines show the dispersions when no NIR data are included. The dispersion in the K_{RB} for ESSENCE increases dramatically at low redshift because R_{4m} is redder than rest frame B, and there are therefore no observations to anchor the SED template on the blue side to which we are transforming. Our lowest redshift ESSENCE object in this analysis is at $z = 0.34$. At the high-redshift end, the uncertainty for K_{IV} is higher since I_{4m} is shifted to the blue side of rest i, and there is no anchor on the red side. Adding the NIR photometry helps in the color matching and decreases the dispersion. There is little effect on the SNLS dispersions because our CSP sample includes only objects with redshifts less than 0.8 and the z_m band serves as a red anchor over this entire range.

(A color version of this figure is available in the online journal.)

photometry. Light-curve templates are then fit to the N filters for which there is optical and NIR photometry yielding $N - 1$ colors as a function of epoch. We then construct a smooth function $S(\lambda)$ which, when multiplied by the template SEDs, yield synthetic colors equal to the observed colors; i.e., we model the template rather than the (more noisy) observed colors. Finally, these improved SEDs are used in Equation (3) to compute the final K-corrections. This color-matching simultaneously accounts for the intrinsic color variations from SN Ia to SN Ia as well as reddening corrections due to dust.

Hsiao et al. (2007) demonstrate that while K-corrections are determined mainly by broadband colors, accounting for differences in spectral features is also necessary. These corrections are based on a larger library of spectra, with a greater number of epochs and wavelength coverage than previously available. They include 67 spectra from the CSP (34 of which cover the I band), obtained at the DuPont telescope, and made available to Hsiao et al. for this purpose. Overall, this new library contains many more spectra with red wavelength coverage, and the telluric features at $\lambda \simeq 6880$ Å, 7200 Å, 8200 Å, and 9400 Å have been identified and removed. In the I band, the Hsiao et al. template includes approximately 250 spectra. Determining accurate K-corrections in the i band requires careful attention to the broad Ca II triplet P-Cygni absorption feature (8498 Å, 8542 Å, and 8662 Å). Fortunately, for the purposes of the CSP, it is only well after maximum light has occurred that the Ca II feature changes dramatically (Hsiao et al. 2007, see Figure 5). Currently, in the spectral region of the i band, 125 spectra have been used for the K-correction template. We are continuing to acquire additional spectroscopy of our low-redshift candidates, specifically to improve the K-corrections as a function of both epoch and decline rate of the SNe Ia.

We show in Figure 5 typical crossband K_{iY} and K_{iJ} corrections based on the Hsiao et al. (2007) library, plotted as a function of time since maximum light at B, for redshifts 0.2, 0.3, 0.45, and 0.6. For comparison, we also show the K-corrections from Nugent et al. (2002). Given the currently larger number of available I-band spectra, and correction for the presence of telluric features, we have adopted the newer K-corrections from Hsiao et al. for the purposes of this study. The greatest differences

occur at early times, 10 days before peak magnitude. The corrections are greatest at late times in the SN Ia evolution, as well as very early times for $z = 0.6$. For our observations around peak magnitude, the K-corrections at these redshifts range from -0.5 to -0.3 magnitudes in Y band and from -1.1 to -0.9 magnitudes in J band. Table 3 contains our currently adopted values for the K_{iY}- and K_{iJ}-corrections. In order to estimate the uncertainties in the K-corrections, we apply the same procedure to the SNe Ia whose spectra were used to generate the template SEDs themselves. For those epochs with spectra, we can compute the K-corrections using the color-matched SED and the observed library spectrum, and compare the results. For each redshift, we compute synthetic photometry and K-corrections based on the library spectrum and appropriately redshifted filter functions, simulating what would be observed if this SN Ia were at redshift z. The SED template is then color-matched to these synthetic observed colors and the K-correction computed again. This is repeated for each library spectrum and the rms difference between the library and template K-corrections is computed. Since ESSENCE, SNLS, and SDSS-II have three different filter sets, we have separately computed the uncertainties in each case.

In Figure 6, we plot the statistical dispersion in the K-corrections as a function of redshift for the filters used in ESSENCE, SDSS-II, and SNLS. The dispersion is sensitive to the filter set used, which determines the accuracy with which we can color-correct the template SED. As expected, the dispersions are lowest at the redshifts where the observed and rest-frame filters overlap and increase at higher and lower redshifts. The largest uncertainties arise when there are no filters to anchor the blue side of the SED at low redshifts or, alternatively, the red side at high redshifts. For comparison, we plot the dispersions

Table 3
CSP High-z Photometry

Name	MJD[a] (days)	Y_c (mag)	σ_Y (mag)	$K_{Y,I}$[b] (mag)	J_c (mag)	σ_J (mag)	$K_{J,I}$[c] (mag)
SNLS 03D4gl	52947.0	22.57	0.09	−0.97	22.84	0.15	−1.37
	52947.0	22.54	0.05	−0.91	23.03	0.13	−1.40
	52952.0	22.64	0.05	−0.90	22.80	0.08	−1.38
SNLS 04D1oh	53302.1	...	...	...	22.81	0.09	−1.39
	53314.2	...	...	...	22.78	0.10	−1.37
SNLS 04D1pg	53328.2	...	...	...	22.72	0.08	−1.46
	53338.1	...	...	...	22.95	0.08	−1.48
	53344.2	...	...	...	23.28	0.19	−1.59
SNLS 04D1rh	53356.1	22.44	0.06	−1.21	22.26	0.07	−1.34
	53356.1	22.60	0.09	−1.23	22.53	0.11	−1.46
SNLS 04D1sk	53356.1	...	...	...	23.33	0.19	−1.50
	53363.0	...	...	...	23.78	0.33	−1.51
SNLS 04D2an	53027.2	22.75	0.05	−1.11	22.92	0.07	−1.41
	53027.2	22.63	0.05	−1.08	23.23	0.11	−1.40
	53034.1	22.84	0.10	−1.03	23.07	0.14	−1.39
	53034.1	22.67	0.05	−0.95	23.58	0.17	−1.39
	53040.2	23.11	0.07	−0.91	23.64	0.17	−1.41
	53040.2	23.27	0.12	−0.90	23.52	0.22	−1.41
	53045.2	23.32	0.07	−1.03	23.38	0.14	−1.41
	53045.2	23.33	0.10	−1.06	23.73	0.20	−1.41
SNLS 05D1dn	53641.3	...	...	...	22.76	0.13	−1.35
	53654.3	...	...	...	22.64	0.10	−1.35
	53659.2	...	...	...	22.94	0.13	−1.36
	53666.2	...	...	...	23.11	0.19	−1.41
SNLS 05D1hk	53720.0	21.10	0.03	−1.02	...	...	...
	53724.1	21.13	0.03	−0.98	...	...	...
SNLS 05D1hn	53721.0	20.63	0.03	−0.97	...	...	...
SNLS 05D1ix	53720.1	...	...	...	22.07	0.09	−1.54
	53722.1	...	...	...	22.27	0.09	−1.54
	53724.0	...	...	...	22.04	0.09	−1.51
SNLS 05D1iy	53721.1	21.65	0.02	−0.92	...	...	...
SNLS 05D2ah	53390.2	20.84	0.03	−0.86	21.46	0.05	−0.39
	53390.2	20.93	0.02	−0.87	...	...	...
	53391.2	...	...	...	21.71	0.06	−0.38
	53392.2	20.93	0.02	−0.92	21.71	0.08	−0.37
	53393.3	21.02	0.03	−0.95	21.77	0.07	−0.37
	53393.3	20.93	0.02	−1.16	21.66	0.04	−0.37
SNLS 05D2bt	53405.1	...	...	...	22.98	0.09	−1.54
	53413.2	...	...	...	23.28	0.24	−1.55
	53418.1	...	...	...	23.07	0.34	−1.56
	53424.1	...	...	...	23.47	0.28	−1.54
	53430.1	...	...	...	23.09	0.20	−1.54
SNLS 05D2bv	53405.3	...	...	...	22.21	0.04	−1.35
	53413.2	...	...	...	22.64	0.13	−1.36
	53418.2	...	...	...	22.58	0.08	−1.41
	53424.2	...	...	...	22.76	0.15	−1.58
	53430.1	...	...	...	22.90	0.14	−1.60
SNLS 05D2ck	53418.3	...	...	...	23.28	0.25	−1.54
	53424.3	...	...	...	23.29	0.30	−1.58
	53430.2	...	...	...	23.51	0.23	−1.59
	53444.1	...	...	...	23.61	0.20	−1.55
SNLS 05D2dw	53447.1	21.99	0.07	−1.16	22.20	0.09	−1.31
	53447.1	22.20	0.06	−1.14	22.00	0.06	−1.30
SNLS 05D2eb	53447.1	22.23	0.12	−0.82	22.40	0.15	−1.51
	53447.1	22.49	0.04	−0.78	...	...	...
SNLS 05D2mp	53720.3	22.44	0.04	−0.94	...	...	...
	53722.2	22.55	0.04	−0.95	...	...	...
	53724.3	22.54	0.04	−0.96	...	...	...
SNLS 05D4cw	53591.1	22.35	0.07	−1.01	...	...	...
	53596.1	22.66	0.08	−1.03	...	...	...
	53608.1	22.55	0.08	−1.05	...	...	...
SNLS 05D4fo	53648.1	22.14	0.45	−1.00	22.07	0.15	−1.35
	53648.1	22.32	0.07	−1.00	21.64	0.06	−1.50
	53654.1	22.50	0.12	−1.00	21.79	0.11	−1.48
	53654.1	22.76	0.10	−1.00	21.96	0.11	−1.56

Table 3
(Continued)

Name	MJD[a] (days)	Y_c (mag)	σ_Y (mag)	$K_{Y,I}$[b] (mag)	J_c (mag)	σ_J (mag)	$K_{J,I}$[c] (mag)
ESS d149wcc4-11	52947.3	22.01	0.04	−0.91	...	...	...
	52952.2	21.92	0.03	−0.92	...	...	...
	52956.2	21.97	0.03	−0.91	...	...	...
ESS e108wdd8-4	52980.1	22.42	0.04	−1.29	22.25	0.08	−1.38
	52980.1	22.24	0.03	−1.30	22.28	0.09	−1.39
	52982.1	22.20	0.03	−1.31	22.28	0.08	−1.39
SDSS 12855	54000.1	20.61	0.02	−0.89	...	...	...
	54008.0	20.92	0.02	−1.10	...	...	...
SDSS 13025	53996.1	21.02	0.03	−1.00	...	...	...
	54000.1	21.08	0.04	−0.99	...	...	...
	54008.1	21.58	0.04	−1.20	...	...	...
SDSS 13835	54008.1	21.14	0.01	−0.90	...	...	...
	54021.2	21.40	0.02	−1.01	...	...	...
SDSS 15287	54029.0	21.13	0.02	−0.94	...	...	...
SDSS 16442	54060.0	21.30	0.04	−0.86	...	...	...
	54065.0	21.46	0.03	−0.80	...	...	...
	54070.0	21.79	0.04	−0.80	...	...	...
SDSS 3241	53641.0	21.31	0.02	−0.86	...	...	...
	53648.0	21.27	0.02	−0.93	...	...	...
	53654.0	21.54	0.02	−0.90	...	...	...
	53659.0	21.79	0.02	−0.95	...	...	...
	53666.0	21.98	0.03	−1.05	...	...	...
SDSS 3331	53641.2	20.80	0.03	−0.88	...	...	...
	53648.3	20.50	0.04	−1.06	...	...	...
	53655.2	20.77	0.03	−1.03	...	...	...
	53659.2	20.82	0.03	−1.10	...	...	...
	53676.2	20.89	0.04	−1.32	...	...	...
SDSS 4679	53655.1	21.99	0.02	−0.89	...	...	...
	53659.1	22.02	0.03	−0.88	...	...	...
	53666.2	22.35	0.04	−0.89	...	...	...
	53676.2	22.37	0.03	−0.91	...	...	...
SDSS 5183	53654.3	22.39	0.06	−1.03	...	...	...
	53655.3	22.46	0.05	−1.04	...	...	...
	53666.2	23.22	0.09	−1.04	...	...	...
	53676.3	22.94	0.07	−1.06	...	...	...
	53720.2	23.68	0.14	−1.09	...	...	...
	53721.2	23.72	0.16	−1.09	...	...	...
SDSS 5549	53666.1	19.88	0.04	−0.56	...	...	...
	53676.1	20.20	0.04	−0.65	...	...	...
	53682.1	20.03	0.11	−0.93	...	...	...
	53684.1	20.18	0.03	−0.95	...	...	...
	53689.1	20.11	0.04	−0.97	...	...	...
SDSS 6699	53676.0	21.72	0.02	−0.90	...	...	...
	53682.0	21.87	0.05	−0.85	...	...	...
	53684.0	22.16	0.04	−0.84	...	...	...
	53689.0	22.42	0.05	−0.85	...	...	...
SDSS 7243	53682.1	20.82	0.02	−0.83	...	...	...
	53684.1	20.87	0.02	−0.88	...	...	...
	53689.0	20.94	0.01	−0.88	...	...	...
SDSS 7512	53682.3	21.21	0.10	−0.89	...	...	...
	53684.3	21.25	0.07	−0.89	...	...	...

Notes.
[a] MJD = JD − 2,400,000.5.
[b] K-correction from observed filter Y_c to rest-frame filter I.
[c] K-correction from observed filter J_c to rest-frame filter I, except for SNLS05D2ah, for which the K-correction is to rest frame Y.

with (solid) and without (dashed) including the NIR photometry; in most cases, the curves overlap and are indistinguishable. In general, the statistical uncertainties in the K-corrections range from ±0.005 to ±0.05 mag. The largest uncertainty is for d149 at a redshift of 0.34, where the transformation to the B band reaches an uncertainty of ±0.1. Similarly, for four SDSS

Table 4
Derived Light-curve Parameters for Low-z SNe

Name	z	$\mu(\sigma)$[a] (mag)	$T_{max}(\sigma)$[b] (days)	$\Delta m_{15}(\sigma)$[c] (mag)	$(i_{max})(\sigma)$[d] (mag)	$(B_{max} - V_{max})$ (σ)[d] (mag)	$E(B - V)_{host}$ (σ)[e] (mag)	A_{TOT}[f] (mag)
SN2004ef	0.03097	35.499(0.139)	53264.32(0.05)	1.389(0.007)	17.273(0.010)	0.123 (0.007)	0.157 (0.018)	0.214
SN2004eo	0.01569	33.697(0.189)	53278.43(0.05)	1.366(0.012)	15.435(0.016)	0.095 (0.015)	0.129 (0.021)	0.249
SN2004ey	0.01578	34.027(0.190)	53304.15(0.04)	0.954(0.006)	15.459(0.011)	−0.070 (0.008)	−0.003 (0.015)	0.163
SN2004gs	0.02663	35.484(0.142)	53355.78(0.05)	1.550(0.006)	17.391(0.009)	0.202 (0.009)	0.223 (0.022)	0.247
SN2004gu	0.04583	36.484(0.129)	53361.60(0.17)	0.758(0.011)	18.052(0.020)	0.145 (0.021)	0.253 (0.027)	0.268
SN2005ag	0.07937	37.643(0.121)	53413.58(0.08)	0.889(0.007)	19.123(0.011)	0.004 (0.007)	0.085 (0.016)	0.128
SN2005al	0.01239	34.092(0.202)	53430.07(0.11)	1.243(0.010)	15.609(0.015)	−0.089 (0.009)	−0.057 (0.016)	0.012
SN2005el	0.01490	33.967(0.189)	53646.54(0.06)	1.299(0.014)	15.538(0.018)	−0.055 (0.014)	−0.025 (0.020)	0.112
SN2005eq	0.02896	35.489(0.141)	53653.69(0.09)	0.778(0.008)	16.962(0.015)	0.039 (0.010)	0.135 (0.020)	0.215
SN2005hc	0.04591	36.582(0.128)	53666.91(0.08)	0.844(0.008)	18.050(0.014)	0.009 (0.008)	0.095 (0.017)	0.129
SN2005hj	0.05797	36.976(0.127)	53673.54(0.21)	0.739(0.017)	18.462(0.026)	0.067 (0.014)	0.170 (0.023)	0.207
SN2005iq	0.03402	35.891(0.136)	53687.44(0.06)	1.230(0.016)	17.457(0.019)	−0.033 (0.011)	0.005 (0.017)	0.032
SN2005ir	0.07631	37.589(0.127)	53684.50(0.21)	0.875(0.025)	19.086(0.037)	0.027 (0.016)	0.112 (0.022)	0.141
SN2005kc	0.01511	33.871(0.197)	53697.84(0.05)	1.150(0.016)	15.632(0.020)	0.200 (0.014)	0.267 (0.019)	0.409
SN2005ki	0.01919	34.615(0.159)	53705.42(0.04)	1.381(0.007)	16.237(0.010)	−0.031 (0.010)	−0.010 (0.019)	0.029
SN2005M	0.02200	35.052(0.151)	53405.40(0.02)	0.799(0.003)	16.518(0.006)	0.024 (0.004)	0.117 (0.017)	0.146
SN2005na	0.02630	35.118(0.145)	53739.83(0.17)	1.005(0.013)	16.618(0.020)	−0.018 (0.015)	0.048 (0.019)	0.137
SN2006ax	0.01673	34.324(0.169)	53826.96(0.06)	0.949(0.008)	15.763(0.014)	−0.060 (0.011)	0.009 (0.017)	0.068
SN2006bh	0.01084	33.329(0.238)	53833.13(0.04)	1.387(0.008)	14.977(0.010)	−0.007 (0.009)	0.016 (0.018)	0.047
SN2006gt	0.04474	36.441(0.130)	54002.54(0.11)	1.675(0.012)	18.415(0.020)	0.225 (0.020)	0.234 (0.031)	0.264
SN2006py	0.05786	36.839(0.137)	54070.50(0.32)	1.016(0.049)	18.421(0.060)	0.070 (0.021)	0.142 (0.025)	0.205

Notes.
[a] Distance modulus ($h = 0.72$).
[b] Time of maximum for rest-frame B light curve (JD − 2,400,000.5).
[c] Decline-rate parameter.
[d] Galactic reddening from Schlegel et al. (1998).
[e] Host galaxy reddening assuming Phillips et al. (1999) colors.
[f] Total (galactic + host galaxy) absorption in NIR toward SN assuming $R_V = 1.7$.

objects at $z < 0.25$ (SN 3331, 5549, 7243, and 7512), the uncertainties also reach ±0.1 mag. For the SNLS objects, the statistical uncertainties in the K-corrections are generally less than ±0.04 mag. The errors for individual epochs for a given object are correlated, and a combined, weighted uncertainty is applied to the distance modulus (or peak magnitude). These uncertainties are included in the total statistical uncertainties computed for each individual SN Ia. We carry these uncertainties in the analysis of cosmological parameters described throughout this paper. Fortunately, progress is continuing to be made in improving K-corrections for SNe Ia. The spectral library will continue to grow in the next few years with additional spectra from numerous groups, including the low-redshift CSP.

5.2. Extinction Corrections

Correcting accurately for extinction remains a challenge for SN Ia cosmology. The issue is complicated by many factors.

1. There are at least four separate potential sources of dust: (a) foreground (Milky Way Galaxy) dust, (b) dust within the host galaxy, (c) dust associated with the circumstellar material of the SN progenitor, and (d) dust in the intergalactic medium.
2. There is no a priori knowledge of the dust properties in the latter three of these environments and the reddening laws could, in principle, be different in all three environments, perhaps being a function of metallicity, atmospheric environment of the SN Ia, or even evolving as a function of time.
3. Even if the extinction law(s) is(are) known perfectly, correcting for reddening requires knowledge of the intrinsic

colors (and their dispersion) to derive a reddening curve. The observed color of a SN Ia is determined by the intrinsic SED of the SN Ia, reddening due to dust, and the expansion of the universe (the K-correction). Hence, there is an inherent circularity in the problem, and generally some assumptions are made (e.g., that the intrinsic colors of SNe Ia are known, and that they are known as a function of redshift and environment, and/or that the reddening law is universal). At present, for SNe Ia, it is still not possible to distinguish unambiguously between a different reddening law and differing intrinsic colors.

The reddening law can be characterized by a ratio of total-to-selective absorption, R_λ, which generally increases toward shorter wavelengths: $R_\lambda = A_\lambda/E(B - V)$, where A_λ is the total absorption at each wavelength, λ. On average, the ratio of total-to-selective absorption, R_λ decreases from 4.9 at U, to 4.1 at B, 3.1 at V, and 1.7 for the I band in the Galaxy (e.g., Cardelli et al. 1989). For a reddening of, say, $E(B - V) = 0.02$ mag, the corrections to the rest-frame U-band magnitude would be ∼0.10 mag and ∼0.03 mag at I. Thus, longer wavelength observations offer a significant advantage in minimizing systematic effects due to reddening.

In general, it has been concluded that the dust properties in other host galaxies appear to be similar to those in the Milky Way (see, for example Riess et al. 1996, 2004; Phillips et al. 1999; Knop et al. 2003; Jha et al. 2007). To date, no empirical evidence for gray dust has been found (e.g., Knop et al. 2003; Riess et al. 2004, 2007); i.e., larger dust grains with wavelength-neutral effects. However, some studies have indicated that the reddening law for SNe Ia is consistent with $R_V \sim 2.5$, lower than the Galactic reddening law (e.g., Wang et al. 2006). Correcting

Table 5
Derived Light-curve Parameters

Name	z	$\mu(\sigma)$[a] (mag)	$T_{max}(\sigma)$[b] (days)	$\Delta m_{15}(\sigma)$[c] (mag)	$(i_{max})(\sigma)$[d] (mag)	$(B_{max} - V_{max})(\sigma)$[d] (mag)	$E(B-V)_{host}(\sigma)$[e] (mag)	A_{TOT}[f] (mag)
SNLS 03D4gl	0.571	42.765(0.170)	52954.12(0.57)	0.719(0.151)	24.192(0.120)	0.020 (0.029)	0.122 (0.038)	0.136
SNLS 04D1oh	0.59	42.680(0.180)	53306.90(0.44)	0.946(0.069)	24.070(0.087)	−0.026 (0.056)	0.046 (0.058)	0.067
SNLS 04D1pg	0.515	42.353(0.148)	53325.53(0.31)	0.813(0.050)	24.059(0.078)	0.138 (0.029)	0.238 (0.034)	0.248
SNLS 04D1rh	0.435	41.942(0.134)	53349.22(0.42)	0.877(0.048)	23.353(0.069)	−0.007 (0.019)	0.074 (0.024)	0.100
SNLS 04D1sk	0.6634	43.307(0.227)	53354.63(0.70)	1.399(0.109)	24.810(0.153)	−0.032 (0.062)	−0.013 (0.066)	0.011
SNLS 04D2an	0.62	42.957(0.151)	53031.21(0.85)	0.872(0.098)	24.347(0.110)	...	...	...
SNLS 05D1dn	0.566	42.417(0.153)	53647.34(0.64)	0.742(0.044)	23.941(0.091)	0.062 (0.031)	0.165 (0.036)	0.181
SNLS 05D1hk	0.2631	40.438(0.176)	53718.13(0.28)	0.889(0.029)	21.926(0.136)	0.027 (0.014)	0.109 (0.021)	0.130
SNLS 05D1hn	0.1489	39.128(0.244)	53713.17(0.12)	0.850(0.038)	21.231(0.219)	0.317 (0.020)	0.428 (0.026)	0.436
SNLS 05D1ix	0.49	42.022(0.131)	53718.61(0.04)	0.896(0.017)	23.526(0.070)	0.034 (0.006)	0.116 (0.016)	0.133
SNLS 05D1iy	0.2478	40.509(0.149)	53715.46(0.07)	1.191(0.041)	22.216(0.096)	0.089 (0.017)	0.142 (0.021)	0.165
SNLS 05D2ah	0.184	39.656(0.104)	53382.54(0.05)	0.995(0.010)	21.310(0.016)	0.090 (0.005)	0.166 (0.014)	0.178
SNLS 05D2bt	0.679	43.169(0.189)	53400.79(0.28)	0.941(0.076)	24.306(0.115)	−0.142 (0.051)	−0.080 (0.054)	−0.056
SNLS 05D2bv	0.474	42.194(0.131)	53403.80(0.07)	1.031(0.037)	23.471(0.065)	−0.089 (0.011)	−0.033 (0.017)	−0.016
SNLS 05D2ck	0.698	43.088(0.256)	53415.75(0.76)	1.644(0.108)	24.721(0.103)	−0.004 (0.097)	−0.010 (0.101)	0.006
SNLS 05D2dw	0.417	41.933(0.123)	53453.29(0.14)	0.879(0.029)	23.240(0.059)	−0.056 (0.013)	0.021 (0.020)	0.043
SNLS 05D2eb	0.5344	42.376(0.218)	53450.37(0.38)	0.836(0.056)	23.885(0.182)	0.043 (0.024)	0.133 (0.030)	0.140
SNLS 05D2mp	0.3537	41.577(0.115)	53710.20(0.08)	0.804(0.014)	23.018(0.054)	0.016 (0.010)	0.108 (0.019)	0.125
SNLS 05D4cw	0.375	41.394(0.174)	53580.99(0.91)	1.396(0.126)	22.920(0.097)	−0.021 (0.048)	−0.000 (0.053)	0.030
SNLS 05D4fo	0.373	41.689(0.120)	53658.00(0.08)	1.269(0.025)	23.232(0.063)	0.003 (0.011)	0.041 (0.018)	0.069
ESS d149wcc4-11	0.342	41.337(0.121)	52955.29(0.29)	0.894(0.045)	22.791(0.038)	0.011 (0.026)	0.091 (0.030)	0.110
ESS e108wdd8-4	0.469	42.391(0.176)	52980.58(0.82)	0.516(0.107)	23.469(0.092)	−0.115 (0.047)	−0.001 (0.055)	0.028
SDSS 12855	0.165	39.423(0.175)	53995.54(0.35)	1.347(0.079)	21.209(0.024)	0.105 (0.041)	0.142 (0.045)	0.196
SDSS 13025	0.224	40.019(0.186)	53993.23(0.85)	1.047(0.089)	21.783(0.081)	0.134 (0.047)	0.208 (0.050)	0.289
SDSS 13835	0.247	40.635(0.156)	54011.01(0.58)	0.816(0.054)	22.002(0.043)	−0.020 (0.037)	0.067 (0.041)	0.093
SDSS 15287	0.235	40.614(0.156)	54028.59(0.36)	0.820(0.065)	21.968(0.056)	−0.026 (0.031)	0.060 (0.035)	0.112
SDSS 16442	0.281	40.217(0.271)	54060.21(1.03)	1.042(0.143)	21.983(0.143)	0.136 (0.092)	0.210 (0.094)	0.284
SDSS 3241	0.259	40.827(0.197)	53647.17(0.37)	1.005(0.056)	21.970(0.053)	−0.148 (0.067)	−0.093 (0.069)	0.079
SDSS 3331	0.208	39.746(0.182)	53649.45(0.35)	0.922(0.070)	21.479(0.064)	0.136 (0.046)	0.224 (0.048)	0.255
SDSS 4679	0.333	41.454(0.235)	53652.66(0.63)	0.704(0.052)	22.734(0.064)	−0.045 (0.093)	0.052 (0.095)	0.084
SDSS 5183	0.384	42.069(0.390)	53649.32(1.26)	0.946(0.130)	23.149(0.133)	−0.170 (0.163)	−0.110 (0.164)	0.042
SDSS 5549	0.119	38.745(0.123)	53665.51(0.41)	0.920(0.047)	20.333(0.054)	0.069 (0.022)	0.152 (0.026)	0.182
SDSS 6699	0.311	41.063(0.194)	53675.42(0.65)	1.075(0.081)	22.468(0.070)	−0.036 (0.067)	0.021 (0.069)	0.085
SDSS 7243	0.204	40.148(0.170)	53685.71(0.22)	0.929(0.066)	21.561(0.053)	−0.013 (0.037)	0.062 (0.040)	0.178
SDSS 7512	0.22	40.353(0.203)	53681.81(0.38)	0.967(0.112)	21.902(0.114)	0.045 (0.047)	0.121 (0.050)	0.235

Notes.
[a] Distance modulus ($h = 0.72$).
[b] Time of maximum for rest-frame B light curve (JD − 2,400,000.5).
[c] Decline-rate parameter.
[d] Galactic reddening from Schlegel et al. (1998).
[e] Host galaxy reddening assuming Phillips et al. (1999) colors.
[f] Total (galactic + host galaxy) absorption in NIR toward SN assuming $R_V = 1.7$.

for SN Ia reddening has generally made use of one or more of the following approaches: (1) using a sample of SNe Ia where the reddening is expected to be negligible in order to define a zero-extinction fiducial sample (e.g., SNe Ia in elliptical galaxies: Hamuy et al. 1996b; Phillips et al. 1999); and/or (2) making use of a discovery by Lira (1995) that after ∼30 days, the $(B − V)$ colors of SNe Ia show a very small dispersion (e.g., Phillips et al. 1999; Prieto et al. 2006; Jha et al. 2007); or (3) not correcting directly for reddening, but solving for a general $(B − V)$ color term that treats the differences in SN Ia intrinsic colors and reddening as indistinguishable (e.g., Tripp 1998; Astier et al. 2006).

We have dealt with the extinction using two different methods. First, we use a "reddening-free" magnitude, as described below. For comparison, we also have solved for the reddening explicitly following Phillips et al. (1999), in which an intrinsic color is assumed for a given value of Δm_{15} and the observed color (after K-corrections and Milky Way reddening corrections are applied) yield the reddening due to the host galaxy. We differ

from Phillips et al. in that we allow for negative reddenings in the models. While a negative reddening is not *physical*, measuring a negative value for the reddening parameter is certainly statistically possible given the uncertainties in the measured photometry, and our uncertainty in the intrinsic dispersion of SN Ia colors. For the whole sample of SNe Ia, the results are statistically unbiased. We list the reddenings, corrected for Galactic foreground reddening, for our individual SNe Ia in Table 4 for the low-z sample and Table 5 for the high-z sample. The mean reddening for the low-redshift sample is $< E(B−V) > = 0.06$ with a standard deviation of 0.09, consistent with that for the high-redshift sample, with $< E(B−V) > = 0.05$ and a standard deviation of 0.10.

We proceed to compute a reddening-free magnitude, w (Madore 1982; Freedman et al. 2001), defined here as:

$$w_{BV}^{i} = i - R_{BV}^{i}(B - V) = i_0 - R_{BV}^{i}(B - V)_0, \qquad (3)$$

where the subscript, 0, refers to intrinsic (unreddened) magnitudes and magnitudes without subscripts are observed magni-

Table 6
Binned Hubble Diagram

$\langle z \rangle$	N	$\langle \mu \rangle$	$\sigma(\mu)$
0.01	6	33.906	0.018
0.02	3	34.635	0.049
0.03	5	35.505	0.028
0.05	5	36.619	0.032
0.08	2	37.595	0.045
0.13	2	38.930	0.117
0.17	2	39.627	0.099
0.24	10	40.357	0.054
0.35	7	41.397	0.057
0.46	5	41.984	0.065
0.56	5	42.543	0.075
0.68	3	43.023	0.107

tudes. The reddening coefficient R_{BC}^A is defined as

$$R_{BC}^A \equiv \frac{A_A}{E(B - C)} = \frac{R_A}{R_B - R_C},$$

where $R_{BV}^I = 1.9$ and $R_{BI}^I = 0.8$ for the case of a standard reddening law (with $R_V = 3.1$), while $R_{BV}^I = 1.1$ and $R_{BI}^I = 0.5$ for $R_V = 2.0$ (Cardelli et al. 1989). The advantage of reddening-free magnitudes is that neither the knowledge of either intrinsic color of SNe Ia, nor a sample of unreddened SNe Ia is needed: w_{BV}^i is defined such that the observed and intrinsic combinations of these magnitudes and colors are numerically equivalent. This method is in wide use for Cepheid variables. However, (just as for other methods), the same color coefficient is applied to both the nearby and distant samples. It should be noted that this is equivalent to using the color term, β, of Astier et al. (2006) if the fiducial color of a SN Ia is 0. Indeed, it would simply be a reddening correction if all SNe Ia had zero colors. An advantage of this method is in the case where the reddening is solely due to dust extinction when this approach will correct for it without the need to isolate an unreddened sample. Furthermore, the β coefficient used by other authors will be the reddening coefficient in such a case.

Given the definition of w_{BV}^i, and because we are adopting a single reddening coefficient, it makes no difference to the final results whether we deal with reddening-free magnitudes or reddening-corrected magnitudes; the results are mathematically equivalent. For both methods, we used the high- and low-redshift data to determine the best value of R_V by minimizing the scatter in the Hubble diagram, while simultaneously solving for the best-fit cosmology.

5.3. Other Systematic Uncertainties: Evolution, Metallicity, and Weak Lensing

In addition to the uncertainties in K-corrections and extinction discussed above, there are other potential uncertainties on the luminosities of SNe Ia (e.g., evolution, metallicity, and weak lensing). For completeness, we briefly summarize the observational situation with respect to these effects. It is observed that spiral galaxies host slower decliners, and hence, more luminous SNe Ia (Hamuy et al. 1996b; Riess et al. 1998). In general, brighter SNe Ia occur in bluer, lower luminosity galaxies (Hamuy et al. 2000). In addition, the scatter in the Hubble diagram is observed to be a function of morphological type of the host galaxy (Sullivan et al. 2003). Gallagher et al. (2008) have noted a correlation for nearby E/S0 galaxies such that SNe Ia in older galaxies are fainter than those in galaxies with younger global ages, as estimated from stellar population models. Further, they find that residuals in the Hubble diagram correlate with the host-galaxy metallicity. Constraints on differing individual SN Ia properties are now coming from detailed comparisons of SN Ia spectra (Hook et al. 2005; Balland et al. 2006; Blondin et al. 2006; Riess et al. 2007). To date, these studies have revealed no evidence for significant evolution or metallicity differences. However, there appear to be systematic differences at shorter wavelengths, particularly in the rest-frame ultraviolet (Ellis et al. 2008; Foley et al. 2008). Although empirically such effects appear to be small relative to the cosmological effect being measured (e.g., Hamuy et al. 1995; Riess et al. 2004; Knop et al. 2003; Astier et al. 2006), understanding at what level these factors affect the observed properties of SNe Ia is critical to SNe Ia cosmology. We will return to these questions as more data become available, and we complete the CSP. Finally, we note that the net magnification due to weak lensing is not predicted to be significant at redshifts $z < 0.7$ (Holz 1998), the redshift interval of the CSP sample.

6. LIGHT CURVES AND DECLINE RATES

In Figures 7–10, we present optical and YJ-band light curves for the 35 SNe Ia with host-galaxy subtractions. The YJ-band data and uncertainties are given in Table 3. We also show the optical light-curve data from the SNLS, ESSENCE, and SDSS-II surveys. The solid lines are template light curves, generated as described below. The quality of the light curves in general is quite good, and there is an excellent correspondence between the optical and the NIR data. For the CSP photometry, the average Y-band uncertainties are ± 0.03 mag, ± 0.06 mag (± 0.10 mag at J), rising to ± 0.08 mag (± 0.19 mag at J) for the redshift intervals $0.1 < z < 0.3$; $0.3 < z < 0.5$; and $0.5 < z < 0.7$, respectively.

We make use of our own CSP low-redshift, optical data (Contreras et al. 2009; Folatelli et al. 2009) for comparison with our NIR sample at higher redshifts. The low-redshift sample is currently comprised of 21 well-observed SNe Ia (those labeled "Best Observed" in Table 1 of Folatelli et al. 2009), with redshifts $z > 0.01$, and with $E(B - V) < 0.5$ mag. As described in more detail in C. R. Burns et al. (2010, in preparation), we construct a set of $BVgri$ light-curve templates based on this sample of 21 CSP SNe Ia. We use a technique similar to that of Prieto et al. (2006) to generate the light-curve templates shown in Figures 7–10, and determine the Δm_{15} decline-rate values and time of B maximum using χ^2 minimization. The fits are done in flux space simultaneously for the optical and NIR data. This technique will be refined as additional data are obtained during the low-redshift part of the CSP. As shown in Figure 1, the i-band light curves usually exhibit a second maximum, which can vary in strength from event to event. The variations of the i-band template are included in the error budget when fitting the i-band templates; these become a statistical error when the i-band distance moduli are plotted in the Hubble diagram. As described in Section 5.1, K-corrections were computed by first color-matching the SED from Hsiao et al. (2007) to the light curves at each epoch. Independent coauthors (C.B., G.F., and M.P.) performed a double-blind check of the light-curve parameters (Δm_{15}), the K-corrections, and the reddenings. Our derived light-curve parameters are given in Tables 4 and 5. As discussed earlier, some of the derived $E(B - V)$ values have negative values. Given the measurement uncertainties and color fluctuations of ± 0.06 mag, however, these negative values are not significant.
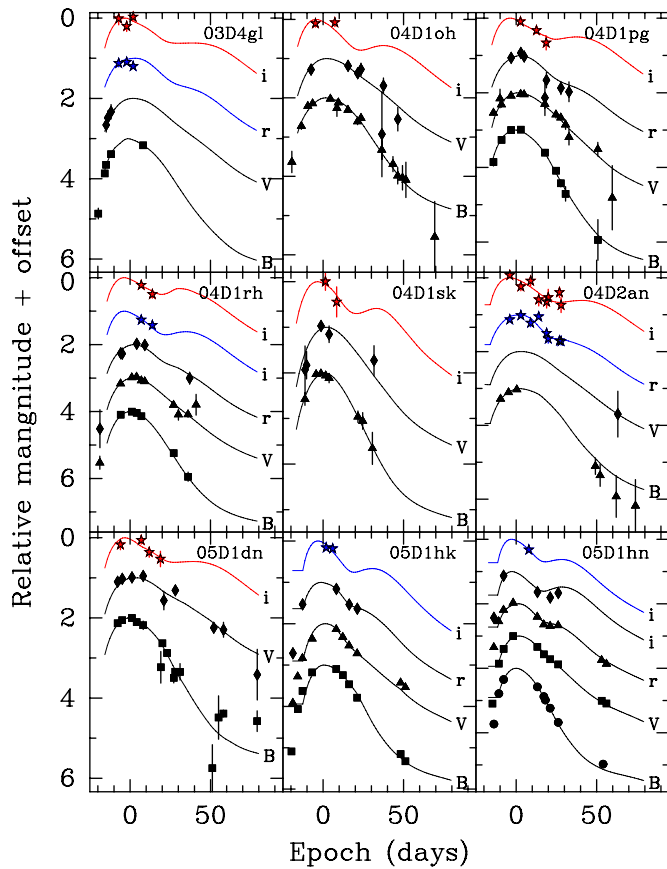
Figure 7. Optical and *YJ*-band light curves for SNe Ia discovered as part of the SNLS, ESSENCE, and SDSS-II projects, followed up using PANIC on Magellan. Light curves and templates are shown in the observer (not rest) frame. The template *BVri* light curves (solid lines) are based on the low-redshift CSP data (Folatelli et al. 2009), and are expanded by $(1 + z)$ and *K*-corrected to fit the observed light curves. The curves are labeled *BVri* to indicate which rest-frame template has been used to fit the observed data. An offset of 1 mag is applied so that the curves do not intersect. In some cases, both the observed *Y* and *J* data are deredshifted to the *i* band. The maximum light magnitudes for each filter are presented in Table 5. The red and blue stars correspond to the CSP's *J*- and *Y*-band data, respectively. The black circles correspond to g_m (SNLS) or g_s (SDSSII); the black squares correspond to r_m (SNLS), r_s (SDSSII), or R_{4m} (ESSENCE); the black triangles correspond to i_m (SNLS), i_s (SDSSII), or I_{4m} (ESSENCE); and the black diamonds correspond to z_m (SNLS).

(A color version of this figure is available in the online journal.)

7. A COMPARISON OF PROPERTIES OF THE CSP LOW- AND HIGH-REDSHIFT SNe Ia

We compare here the rest-frame $(B - V)$ and $(V - i)$ colors for the CSP nearby and high-redshift samples analyzed in this paper. These colors are computed based on the peak magnitudes in each band. In Figures 11 and 12, we show histograms for the 21 nearby SNe Ia ($z < 0.1$) and 35 more distant CSP SNe Ia with $0.12 < z < 0.70$. The mean colors and 1σ dispersions for our sample are $(V - i) = -0.63 \pm 0.12$ mag and $(V - i) = -0.67 \pm 0.16$ mag at low and high redshifts, respectively. For $(B - V)$, the mean colors are $(B - V) = 0.04 \pm 0.09$ mag and $(B - V) = 0.02 \pm 0.10$ mag, respectively. The colors are consistent to within the uncertainties. However, the very red CSP objects SN 2005A and SN 2006X have not been included in this analysis since they do not fit our redshift or reddening criteria, as defined above. In Figure 13, we show a comparison of the distribution of values for Δm_{15} for the low- and high-redshift samples. The mean values for Δm_{15} are 1.11 ± 0.28 and 1.18 ± 0.33 for the nearby and more distant samples,
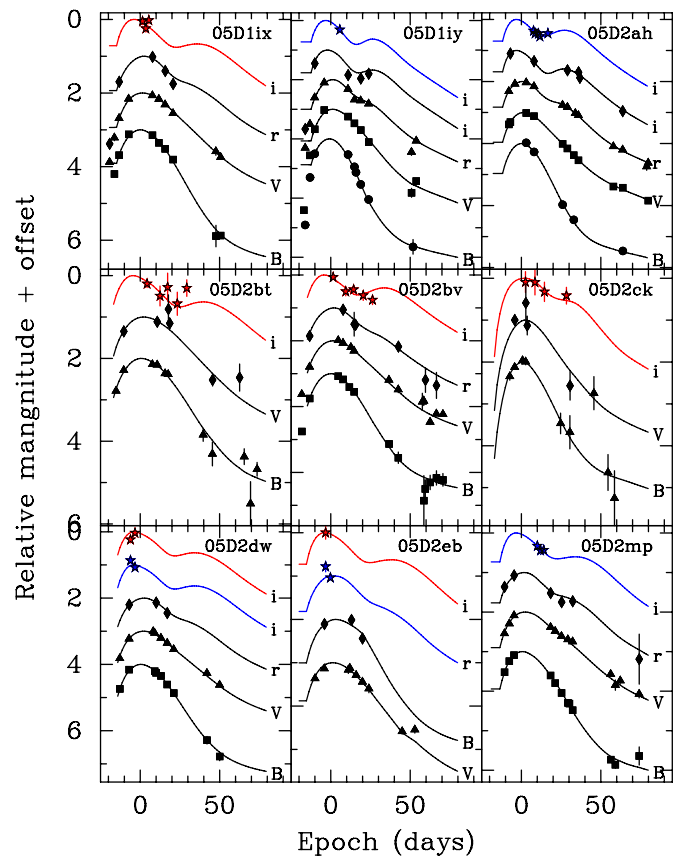
Figure 8. Same as Figure 7.
(A color version of this figure is available in the online journal.)
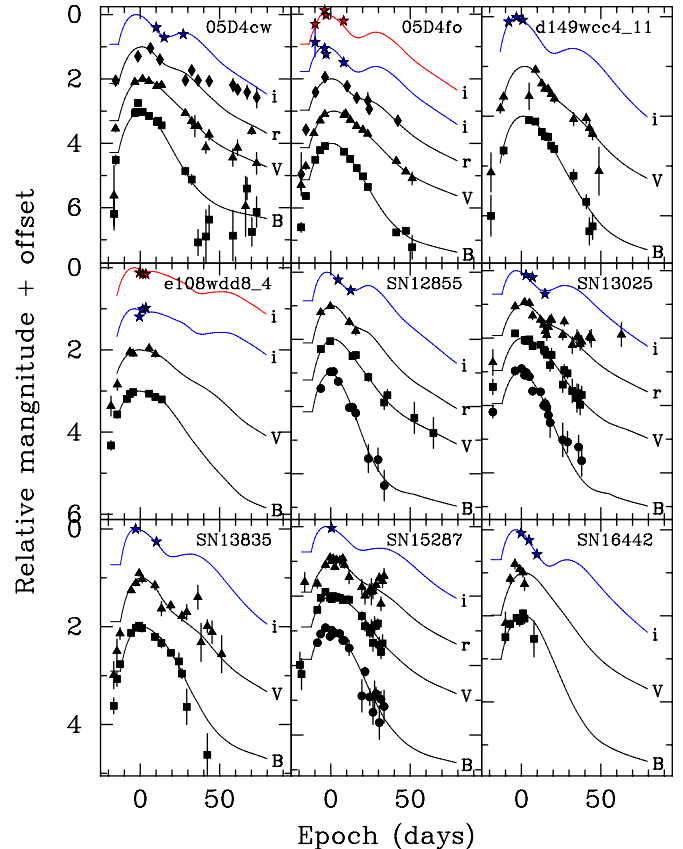
Figure 9. Same as Figure 7.
(A color version of this figure is available in the online journal.)
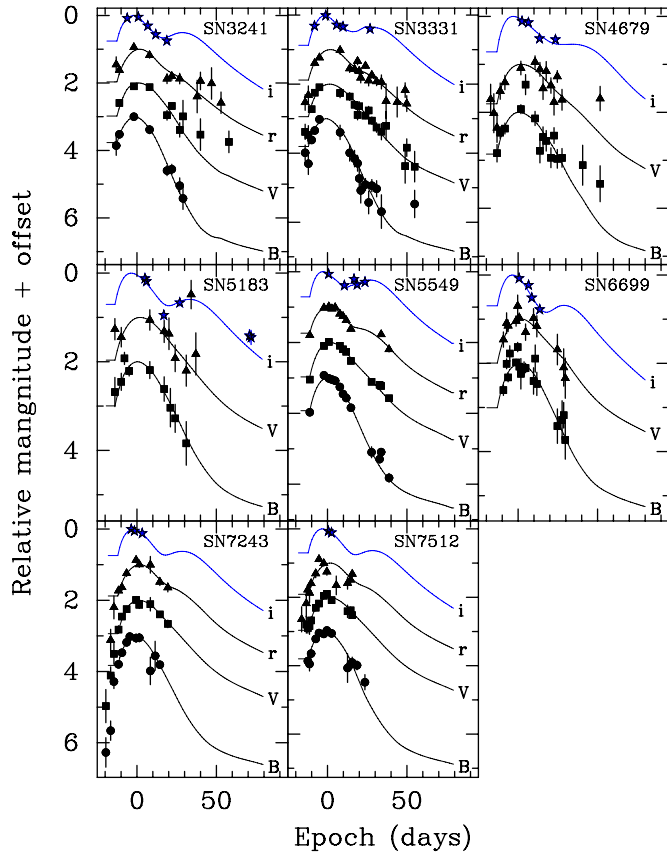
Figure 10. Same as Figure 7.

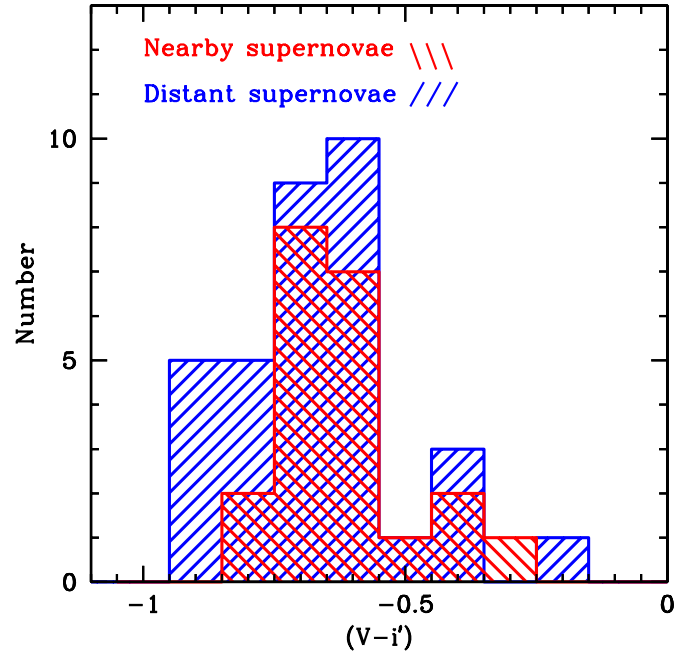(A color version of this figure is available in the online journal.)

Figure 11. Histograms of the $(V-i)$ color distributions at low and high redshifts for the SNe Ia labeled "Best Observed" in Table 1 of Folatelli et al. (2009), with redshifts $z > 0.01$, and with $E(B-V) < 0.5$ mag. Note that the $(V-i)$ colors on our natural system are all negative, and bluer than $(V-I)$. The object SN 04D2an is not included in this plot as it has no rest-frame V observation.

(A color version of this figure is available in the online journal.)
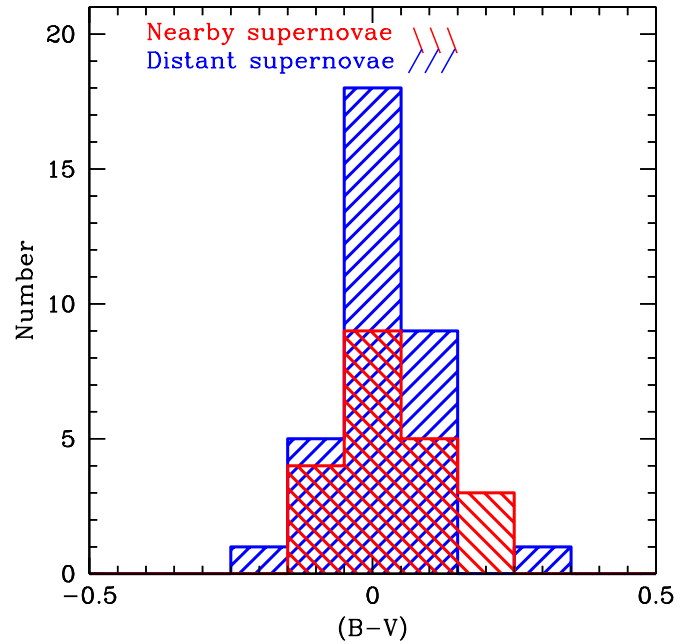
Figure 12. Histograms of the $(B-V)$ color distributions at low and high redshifts.

(A color version of this figure is available in the online journal.)

respectively. There is good overlap in the two distributions, although the distant sample is more peaked. Given the different selection effects for the different samples and the possibility of SN Ia evolution, we do not necessarily expect the low- and high-redshift distributions to agree. For this small sample, quantitative comparison is limited; however, we conclude that the low-redshift sample spans the parameter space of high-redshift color and Δm_{15}.

8. DISTANCE MODULI, REDDENINGS, AND ERRORS

We now turn to the determination of the distance moduli, reddenings, and errors associated with these quantities. We undertake a simultaneous fit for the distance modulus as well as three parameters used to define the absolute magnitudes. We include both the low- and high-z SNe Ia in this analysis. For each independent choice of three filters used to define the reddening-free magnitude (generally BVi), we use the following three parameters to define the absolute luminosity of a SN Ia. We treat these three quantities as nuisance parameters in this analysis:

1. W_0, the absolute reddening-free magnitude of a SN Ia with $\Delta m_{15} = 1.1$;
2. b, the slope of the W–Δm_{15} relation; and
3. R_V, the ratio of total-to-selective absorption.

The absolute (reddening-free) magnitude for a SN is then $W_{BV}^i = W_0 + b\,(\Delta m_{15} - 1.1)$. To compute the distance moduli for the entire sample, we then measure an apparent reddening-free magnitude at maximum light, $w_{BV}^i\,(t_{max})$, for the rest-frame BVi photometric bands. The distance modulus is then, by definition, $\mu_0 = w_{BV}^i - W_{BV}^i$. Distance moduli are listed in

Table 5. (Here, a value of $H_0 = 72$ km s^{-1} Mpc^{-1} is adopted. However, the value of H_0 cancels out for the determination of other cosmological parameters in Section 9.)

Using a reduced $\chi^2 = 1$ approach (Tremaine et al. 2002), we then compute χ^2 by comparing the measured distance modulus, μ_0, with a theoretical distance modulus $\mu_T\,(\mathcal{C})$ where $\mathcal{C}$ represents the set of cosmological parameters (e.g., Ω_m, Ω_{DE}, and w),
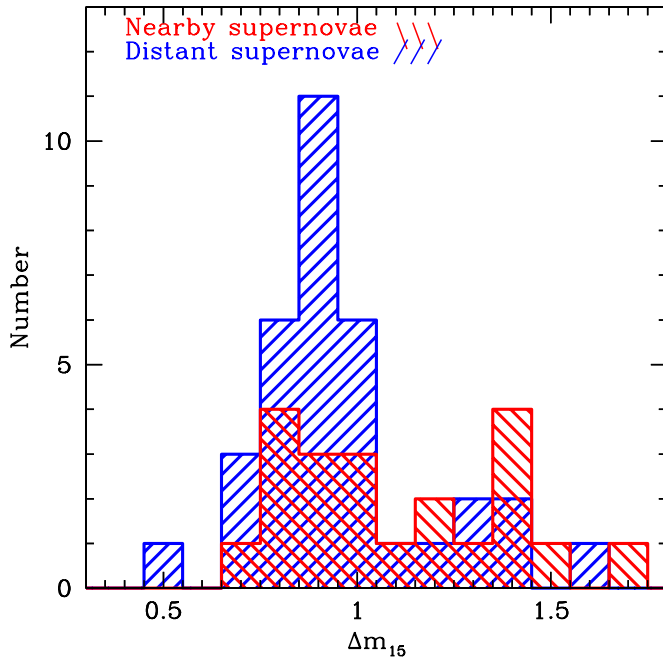
Figure 13. Histograms of the Δm_{15} distributions at low and high redshifts.
(A color version of this figure is available in the online journal.)

we consider:

$$\chi^2 = \sum_j \frac{[\mu_j - \mu_T(\mathcal{C}, z_j)]^2}{\sigma_j^2 + \sigma_{SN}^2}, \tag{4}$$

where σ_{SN} is the intrinsic dispersion of SNe Ia, chosen such that reduced-$\chi^2 = 1$ (for which we find a value of $\sigma_{SN} = 0.09$), and σ_j^2 is the total variance for observation j and is given by

$$\begin{aligned}\sigma_j^2 = {} & \sigma^2(i_{\max}) + R_{BV}^{i2}\sigma^2(B_{\max} - V_{\max}) + b^2\sigma^2(\Delta m_{15}) \\ & - 2R_{BV}^i\sigma(i_{\max}, B_{\max} - V_{\max}) - 2b\sigma(i_{\max}, \Delta m_{15}) \\ & + 2R_{BV}^i b\sigma(B_{\max} - V_{\max}, \Delta m_{15}), \end{aligned} \tag{5}$$

where $\sigma^2(x)$ is the variance in parameter x, and $\sigma(x, y)$ is the covariance between parameters x and y. A peculiar velocity term of ± 300 km s^{-1} is also included. By minimizing this χ^2 (i.e., the residuals in the Hubble diagram), we simultaneously determine the cosmology and the three nuisance parameters W_0, b, and R_V. In this sense, our method is conceptually similar to that described by Tripp & Branch (1999); Astier et al. (2006); and Conley et al. (2008). We defer a discussion of the results for cosmology until Section 9, and discuss first the results for the decline-rate and reddening parameters from this method.

Using the i-band data at maximum, corrected for reddening based on the BV photometry, the results for W_{BV}^i are $W_0 = -18.45 \pm 0.05$ (statistical) ± 0.01 (systematic), $b = 0.38 \pm 0.08$ (statistical) ± 0.01 (systematic), and $R_V = 1.74 \pm 0.27$ (statistical) ± 0.1 (systematic).[27] Since we have data for three filters, we can independently correct for reddening using different combinations of bandpasses (e.g., $B-V$, $V-i$, or $B-i$). However, we prefer to solve for the reddening using simultaneous data from a single photometric/telescope system ($B-V$), which is

available for all of the SNe Ia, rather than a hybrid optical–NIR combination. If, instead, we use the B-band data and correct for reddening based on the BV photometry, W_{BV}^B, we find $W_0 = -19.11 \pm 0.07$, $b = 0.65 \pm 0.13$, and $R_V = 1.66 \pm 0.27$. Encouragingly, R_V is consistent for the two filter combinations. The final results for the cosmology are consistent to within the uncertainties, with all combinations of bandpasses.

A value of $R_V = 1.74$ is significantly lower than a Milky Way value of $R_V = 3.1$. A lower value of R_V is also found by Tripp (1998), Tripp & Branch (1999), and Wang et al. (2006). Conley et al. (2008) and Astier et al. (2006) would find an even lower value than ours, consistent with $R_V (= R_B - 1) \sim 1$ (their $\beta = 2$ would correspond to R_B), if their color term was associated with the extinction law.

As a check on our reddening corrections, two independent analysis methods were used by two of this paper's coauthors (C.B. and G.F.) to determine the nuisance parameters: the reddening-free method outlined above, and the extinction method outlined in Phillips et al. (1999). We initially discovered a large discrepancy between the two derived values of R_V. The reason for this discrepancy can be understood from Equations (4) and (5). The denominator of χ^2 includes terms that depend on both R_V and b. Depending on the magnitude of the variances and covariances, these terms have leverage on the final solution. We have found that a significant issue affecting the derived reddening law is what is assumed for the variance in SNe Ia colors, $\sigma^2(B - V)$, with the value of R_V increasing with increasing $\sigma^2(B - V)$ (see the Appendix). The two analysis methods agree well if consistent errors are adopted. It should therefore be stressed that accurate estimates of the variances in the data are crucial for the determination of R_V. As a further test of these different approaches, C. R. Burns et al. (2010, in preparation) have begun to explore this issue with an unbiased estimator using a Monte Carlo Markov Chain (MCMC). This work goes beyond the scope of the present paper, but we note that the preliminary results agree well with those presented here, with $R_V = 1.8$. Our current analysis and that of Folatelli et al. (2009) are consistent with a picture in which, in addition to corrections for Milky-Way-like dust, there is an intrinsic dispersion in the colors of SNe Ia that is correlated with luminosity, but not the decline rate.

Before concluding this section, it is worth emphasizing that disentangling a possible additional intrinsic color term from extinction leaves open a challenge to SN Ia cosmology. Potential differences in either the intrinsic or observed sample populations of SNe Ia with redshift and/or environment, or differences in the reddening law may limit the ultimate accuracy for cosmology, and for reaching systematic uncertainties significantly below the $\sim \pm 10\%$ level. Having highlighted the remaining challenges, we note, however, that the level of the effect we are discussing amounts to less than $\pm 10\%$, and reaching a systematic uncertainty at this level for SNe Ia is already excellent progress. Few other methods in the use for dark energy measurements currently offer this kind of accuracy. We now turn to a discussion of the Hubble diagram, and then to implications of different values of R_V on the cosmology.

9. HUBBLE DIAGRAM AND COSMOLOGICAL RESULTS

9.1. The First I-band Hubble Diagram for $z > 0.1$

In Figure 14, we show the i- and B-band Hubble diagrams, uncorrected for reddening. The residuals about the best fit to these data are shown in the panels below. We can immediately

---

[27] Unless otherwise noted, all reported uncertainties are statistical and correspond to 1σ errors (68% confidence).
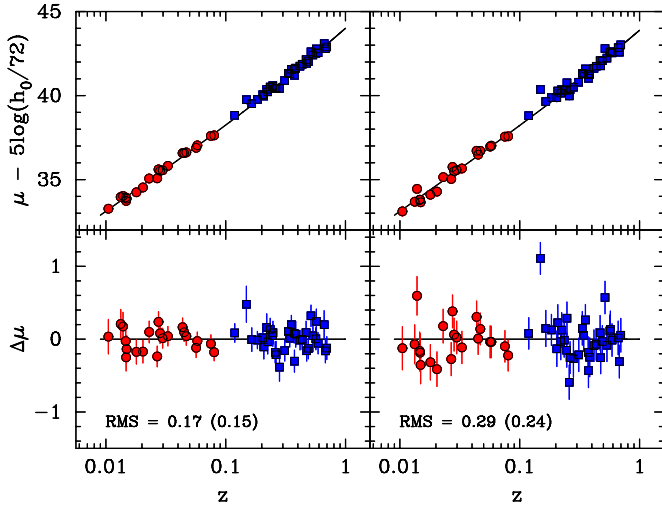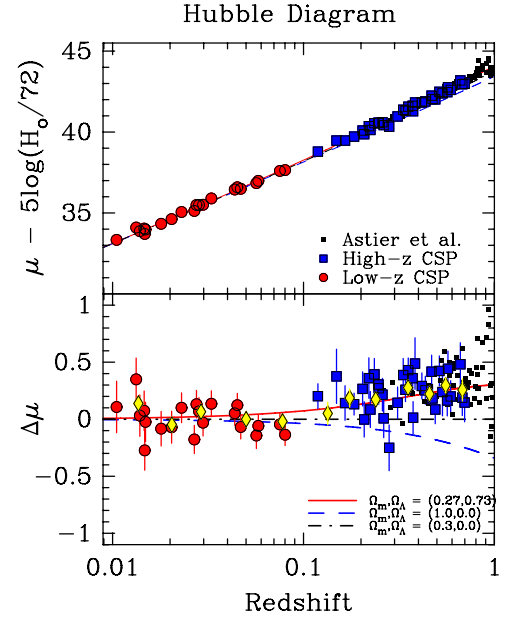
Figure 14. Top panel: *i*- and *B*-band Hubble diagrams for 21 low-redshift and 35 high-redshift SNe Ia from the CSP, *uncorrected for reddening*. Bottom panel: the residuals about the best fit to these data. The values for rms scatter about the best fit to these data are labeled. The rms value in brackets excludes the most discrepant (highly reddened) SNLS 05D1hn.

(A color version of this figure is available in the online journal.)


Figure 15. *i*-band rest-frame Hubble diagram for a total of 56 CSP SNe Ia, 35 SNe Ia from the Magellan CSP sample (blue squares), and 21 low-redshift data (red solid circles) from Folatelli et al. (2009). For comparison, distances determined by Astier et al. (2006) are shown as black squares, but are not included in the fits. Error bars shown are 1σ. A value of $H_0 = 72$ km s^{-1} Mpc^{-1} has been adopted for the plot. The solid (red), dot-dashed (black), and dashed (blue) lines represent $\Omega_m = 0.3$, $\Omega_{DE} = 0.7$; $\Omega_m = 0.3$, $\Omega_{DE} = 0$; and $\Omega_m = 1$ models, respectively. The data are consistent with the standard (accelerating) cosmological model. To minimize the effects of peculiar velocities, the fit to the low-redshift sample is restricted to $z > 0.010$. In the bottom panel, the data are shown relative to the standard model, shown as the solid line. The yellow diamonds are the result of binning the data (see Table 6).

(A color version of this figure is available in the online journal.)

see the advantage of observing SNe Ia at red wavelengths relative to the optical. The rms dispersions in these plots amount to ±0.17 and ±0.29 mag, respectively.

In Figure 15, we present the first *i*-band Hubble diagram for the CSP sample of 35 SNe Ia based on Magellan data (solid blue squares) using the reddening-free magnitude technique described in Section 6, adopting a value of $R_V = 1.74 \pm 0.27$. The error bars shown in the lower panel represent the formal 1σ uncertainties in the distance modulus and include the combined errors in the photometry, the dispersion in the light-curve templates, the estimated dispersion in K-corrections, the error in the foreground Galactic reddening, and the covariances between the light-curve parameters. We also include a peculiar-velocity component of ±300 km s^{-1}. The top curve corresponds to an $\Omega_m = 0.27$, $\Omega_{DE} = 0.73$ cosmology. The yellow diamonds represent the binned data, as given in Table 6. For comparison, the small black squares indicate distance moduli from Astier et al. (2006). The current CSP sample of 21 nearby SNe Ia from Folatelli et al. (2009, solid red circles) is also shown in Figure 15. The low-redshift sample is restricted to nearby SNe Ia in the Hubble flow, having redshifts greater than $z > 0.010$, so that the scatter due to random peculiar velocities is minimized. (The results remain consistent, to within the quoted uncertainties, if we further restrict the sample to $z > 0.015$ or $z > 0.02$.)

The immediate conclusion we can draw from this Hubble diagram is that the CSP data alone provide independent evidence for a (standard) cosmological model with $\Omega_m = 0.3$ and $\Omega_{DE} = 0.7$. The CSP constraints can be further improved by combining them with other independent measurements, for example, baryonic acoustic oscillations (e.g., Eisenstein et al. 2005). A weighted fit to our 35 data points in combination with baryon acoustic oscillations (assuming $w = -1$) yields the solution: $\Omega_m = 0.27 \pm 0.02$(statistical), $\Omega_{DE} = 0.76 \pm 0.13$(statistical) ± 0.09(systematic). The systematic uncertainties for SNe Ia do not have much impact on the determination of Ω_m since this parameter is determined largely by the matter power spectrum. We quote only statistical uncertainties for Ω_m here. The statistical uncertainties are determined by marginalizing over all other parameters and fitting the one-

dimensional probability distribution to a Gaussian. The systematic uncertainties are treated below in Section 9.3.

Based on the fit to the Hubble diagram above, we show, in Figure 16, our error ellipses in the Ω_m–Ω_{DE} plane. Consistent with previous SN Ia studies, we find that based on the SN Ia data alone (and the assumption that $w = -1$), a value of $\Omega_{DE} > 0$ is required at greater than the 99% confidence level.

As an alternative to making assumptions about w, we can use the CSP data to calculate w under the assumption of flatness ($\Omega_k = 0$). Here, we again combine the CSP results with independent measurements of baryonic acoustic oscillations (e.g., Eisenstein et al. 2005), as shown in Figure 17. Assuming a flat cosmology, these joint constraints yield a value of $\Omega_m = 0.27 \pm 0.03$ (statistical) and $w = -1.05 \pm 0.13$ (statistical) ± 0.09 (systematic). For the purposes of this calculation, we are assuming that w is a constant (i.e., $w_a = 0$). These results are in excellent agreement with other joint constraints from SN Ia studies and baryon acoustic oscillations (Astier et al. 2006; Wood-Vasey et al. 2007; Riess et al. 2007), which also yield values of $w = -1$ and $\Omega_m = 0.3$, to within the quoted measurement uncertainties. We have also combined our CSP results with the two-dimensional probability contours from the 2dF galaxy redshift survey (Hawkins et al. 2003). We find $\Omega_m = 0.27 \pm 0.09$ (statistical) and $w_0 = -1.03 \pm 0.23$ (statistical), in good agreement with the SDSS data, but with larger uncertainties on the value of w_0.

In Figure 18, we show a comparison of the residuals in the Hubble diagram for the high-*z* data ($z > 0.10$) for the *i*- and *B* bands relative to the best-fit flat, constant w cosmological
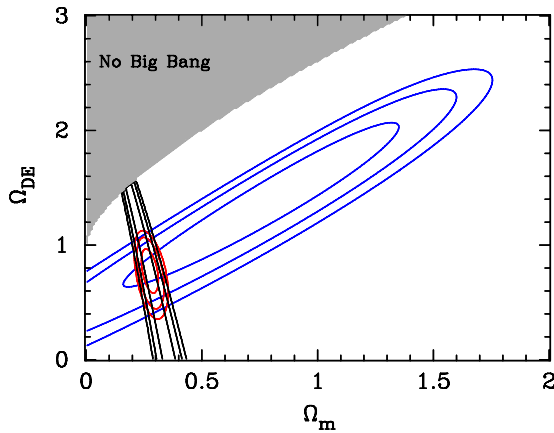
Figure 16. Our best-fit cosmological model in the Ω_m–Ω_{DE} plane assuming a constant equation of state parameter $w = -1$. Our 68%, 95%, and 99% confidence intervals are shown as solid blue (diagonal) contours. The constraints from baryon acoustic oscillations (Eisenstein et al. 2005) are shown as solid black (nearly vertical) contours, and the combined confidence intervals are shown as red contours.

(A color version of this figure is available in the online journal.)
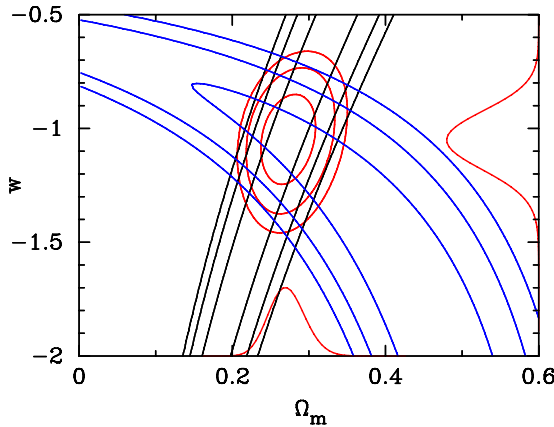
Figure 17. Combining the CSP constraints with baryonic acoustic oscillations (Eisenstein et al. 2005) and assuming $\Omega_k = 0$. The CSP and BAO data combined are consistent with a value of $w = -1.05 \pm 0.13$ (statistical) ± 0.09 (systematic) and $\Omega_m = 0.27 \pm 0.02$ (statistical). Our 68%, 95%, and 99% confidence intervals are shown as solid blue (banana-shaped) contours. The constraints from baryon acoustic oscillations (Eisenstein et al. 2005) are shown as solid black contours, and the combined confidence intervals are shown as red contours. The one-dimensional marginalized probabilities for each parameter are plotted as red lines on the axes.

(A color version of this figure is available in the online journal.)

model, again for a value of $R_V = 1.74$. The rms scatter in the i-band Hubble diagram amounts to ± 0.13 mag about the fit; the B-band scatter amounts to ± 0.15 mag.[28] The resulting cosmological parameters are in good agreement, with differences in w and Ω_m amounting to only 0.03 and 0.01, respectively, well within the measurement uncertainties. The i-band measurements have smaller systematic uncertainties due to smaller reddening corrections, and also have somewhat smaller observed scatter.

As discussed in Section 6, we find that the smallest scatter in the Hubble diagram at low (as well as high) redshift is found for a value of the (color coefficient or) ratio of total-to-selective absorption $R_V = 1.74 \pm 0.27$. The standard Galactic

---

[28] The rms values exclude SN 04D2an at a redshift of $z = 0.62$, which has no reliable rest-frame V-band observation and therefore no color correction is possible using only the optical data.
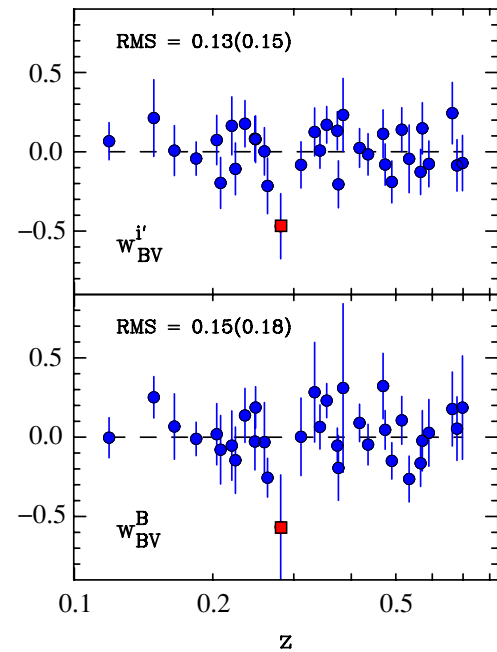
Figure 18. Residuals in the i and B Hubble diagrams. The top panel shows reddening-free i magnitudes, and the bottom panel shows the reddening-free B magnitudes. Both are computed using the $(B - V)$ color. The rms dispersion is shown in the upper left. SN 04D2an is not shown as it has no V-band observation. If one includes SN 16442 (red square), the dispersion in the Hubble diagram increases to ± 0.15 at i, and ± 0.18 at B as indicated in parentheses. The dashed line corresponds to the best-fit cosmological model.

(A color version of this figure is available in the online journal.)

Table 7
Cosmological Results

R_V	Band	Ω_m	w	rms
1.74	$W_{BV}^{i'}$	0.27 ± 0.02	-1.05 ± 0.13	0.13
	W_{BV}^{B}	0.27 ± 0.02	-1.08 ± 0.14	0.15
3.1	$W_{BV}^{i'}$	0.26 ± 0.02	-1.20 ± 0.13	0.20
	W_{BV}^{B}	0.25 ± 0.03	-1.24 ± 0.16	0.24

reddening law is $R_V = 3.1$. In Table 7, we show the fits to Ω_m and Ω_{DE} and the rms scatter about the cosmological fit for two values of R_V, 1.74 and 3.1, for both the i- and B-band data. For an adopted value of $R_V = 1.74$, the resulting values of Ω_m and w are in excellent agreement between both bands. However, adopting instead a value $R_V = 3.1$ results in a value of $w = -1.20 \pm 0.13$ for the i data and $w = -1.24 \pm 0.16$ for the B data. The solutions for these different adopted values of the reddening are still mutually consistent, but the scatter in the Hubble diagram increases by about 50% for $R_V = 3.1$. Given the increase in the Hubble diagram scatter at larger redshifts for values of $R_V = 3.1$, and the excellent fit to the low redshift CSP sample for $R_V = 1.74$, we conclude that currently the CSP data are consistent with a lower value of a color coefficient and/or reddening law.

It is interesting to ask what happens if reddening effects are ignored altogether. In this case, we find (based on the data shown in Figure 14), that for i, $\Omega_m = 0.29 \pm 0.03$ (statistical) and $w_0 = -0.90 \pm 0.14$ (statistical), consistent to within the systematic uncertainties with the results from the reddening-free and reddening-corrected data discussed above. For the B-band data, however, $\Omega_m = 0.31 \pm 0.03$ (statistical), $w_0 = -0.70 \pm 0.21$ (statistical), and the results for the equation

of state are much more sensitive to the treatment of reddening. These results quantitatively illustrate the advantage of the *i* band in minimizing systematic effects for SNe Ia cosmology. We have also shown that the *i* band can be calibrated as well as the *B* band; in fact, there is a further advantage to the *i* band, where the luminosity–Δm_{15} relation has a smaller slope.

It is beyond the scope of this paper to unambiguously ascertain the reddening properties for SNe Ia; however, we make the following observations. The simplest assumption, the application of a standard reddening law coefficient, $R_V = 3.1$ alone, does not provide the best fit to either the low redshift or high redshift CSP data as defined by reduced scatter in the Hubble diagram. As previously noted, this in and of itself does not imply a different reddening law within the host galaxies. For example, it could be indicating an intrinsic color term or perhaps an unusual kind of reddening resulting from dust in the vicinity of the SN Ia. In fact, it would be a somewhat unusual circumstance for the dust within the interstellar medium of all SN Ia host galaxies to have different properties from the dust in nearby galaxies; e.g., LMC, SMC, and the Milky Way, which are the only galaxies for which the value of R_V can be measured to high accuracy and where on average it is found to be equal to 3.1 (Draine 2003). Nobili and Goobar (2008) have determined the average reddening law for a sample of 80 SNe Ia and find that it agrees with Cardelli et al. (1989) for R_V 1.75 ± 0.27. It has also recently been shown that normal dust which is distributed locally around the SN can produce a reddening law with lower value of R_V (Goobar 2008). In other words, this abnormally low value of R_V may simply be due to the geometry of local dust around the SN, which dominates any extinction produced by the host galaxy.

We plan a detailed investigation of the reddening law for SNe Ia based on our low-redshift CSP sample, which was designed to provide independent determinations of reddening at multiple wavelengths. For the present discussion, we adopt a general color coefficient term consistent with a reddening law (or color term), $R_V = 1.74 \pm 0.27$.

9.2. Dark Energy and Other Parameterizations of the Expansion

How do we best compare the observational SN Ia data with cosmological models? While a simple question, this issue is nontrivial. As discussed in Section 1, the expansion of the universe can be parameterized in terms of the equation of state parameter, *w*. Lacking a physical explanation for the dark energy, this is a helpful parameterization, but it is still just that—a parameterization. It is important to keep in mind what the actual observables are–observations yield magnitudes and redshifts–not accelerations, equations of state, or second derivatives of scale factors (the deceleration parameter). In the case of a flat universe, the luminosity distance is given by

$$d_L(z) = r(z)(1 + z) = \int_0^z \frac{z'}{H(z')}, \qquad (6)$$

where $r(z)$ is the comoving distance. Because the luminosity distance relates (inversely) to the *integral* of $H(z)$, it does not provide information on how the expansion rate may have changed from higher redshifts to today. A model is required to infer this evolution.

We now turn to a discussion of the equation of state parameter, *w*, which is commonly used in current cosmological models. A number of ways to parameterize *w* have been suggested in

the literature (e.g., Linder 2006; Albrecht et al. 2006). The functional forms for the evolution in *w* have included simple terms that are either linear functions of redshift, *z* (or scale factor, *a*), but range also to more exotic functional forms. It must be emphasized that while SN Ia data alone provide a very strong case for a nonzero value for Ω_{DE} (i.e., an additional component to matter and radiation), SN Ia data *alone* do not provide a sensitive means of constraining either the value of *w* at the current epoch, or its time evolution.

As discussed in Section 9.1, under the assumption of flatness ($\Omega_k = 0$), SNe Ia can provide a strong constraint on *w* when combined with another experiment like baryon acoustic oscillations. Given current evidence, flatness is not an unreasonable assumption; for example, we note that either recent H_0 or SNe Ia results, in combination with the *WMAP* observations, yields $\Omega_k = -0.01 \pm 0.01$ (Spergel et al. 2007). However, additional methods (e.g., baryon acoustic oscillations, cluster growth, and weak lensing) must be combined with the SN Ia data to provide meaningful constraints on *w*. At the current time, the accuracy required is not yet sufficient for any of these methods alone, and is the goal of future studies.

The cosmological parameterization (Ω_m, Ω_{DE}, and *w*) rests on assumptions about the matter/energy content of the universe and the functional form for the dark energy equation of state. Here, we also investigate another parameterization that is independent of this theoretical framework and involves a purely kinematic model described by the three parameters: (q_0, j_0, Ω_k). Here $q_0 = -\ddot{a}\dot{a}^{-2}a$ is the cosmic deceleration; $j_0 = \dddot{a}\dot{a}^{-3}a^2$ is the third derivative of the scale factor, the so-called cosmic jerk; and Ω_k is the curvature parameter. The only assumption that enters into this parameterization is that the Robertson–Walker metric accurately describes the geometry of the universe. It is therefore free of assumptions about the energy content of the universe or even that the Einstein field equations are the correct description of gravity; it is a purely kinematic model. Although currently somewhat out of fashion, it still remains the closest parameterization of the data, since it is acceleration that is actually being measured. In the standard cosmological model (Ω_m, Ω_{DE}, w) = $(0.3, 0.7, -1)$, $j = 1$, and $q_0 = -0.67$. As noted by Blandford (2004), lacking an understanding of the dynamics of the universe, a purely kinematic description remains a well-motivated family of models to explore.

The scale factor is expanded as a Taylor series:

$$\frac{a(t)}{a(t = t_0)} \simeq 1 + H_0(t - t_0) - \frac{1}{2}q_0 H_0^2 (t - t_0)^2 + \frac{1}{6}j_0 H_0^3 (t - t_0)^3 + \dots, \tag{7}$$

from which one can then derive a luminosity distance. Caldwell & Kamionkowski (2004) provide a convenient expansion of the luminosity distance to third order in *z* and show that to within the precision of this truncation of the Taylor series, the cosmic jerk and the curvature can be combined into one parameter ($j_k = j + \Omega_k$):

$$d_L(z) \simeq \frac{cz}{H_0}\left\{1 + \frac{1}{2}(1 - q_0)z - \frac{1}{6}\left(1 - q_0 - 3q_0^2 + j_0 + \Omega_k\right)z^2 \right.$$
$$\left. + \mathcal{O}\left(z^3\right)\right\}.$$

Using the definitions of these parameters and the Friedmann equation, one can derive the transformation equations between

Table 8
Systematic Errors

Systematic	Error	$\Omega_k = 0$		$w = -1$		$j =$ constant						Nuisance		$\frac{dW_0}{d\sigma}$	ΔW_0
		$\frac{dw}{d\sigma}$	Δw	$\frac{d\Omega_{DE}}{d\sigma}$	$\Delta\Omega_{DE}$	$\frac{dq_0}{d\sigma}$	Δq_0	$\frac{dj_k}{d\sigma}$	Δj_k	$\frac{dR_V}{d\sigma}$	ΔR_V	$\frac{db}{d\sigma}$	Δb		
Mag. offset (δm)	0.025	−2.69	0.067	2.73	0.068	−2.75	0.069	8.10	0.203	0.04	0.001	0.002	0.000	−0.25	0.006
Color offset (δc)	0.02	2.53	0.051	−2.58	0.052	2.68	0.054	−7.77	0.155	0.38	0.008	−0.03	0.001	0.21	0.004
Color term ($\delta(CT)$)	0.015	1.8	0.027	−1.73	0.026	1.83	0.027	−5.82	0.087	−0.67	0.010	−0.22	0.003	0.71	0.011
Δm_{15} variance (σ_Δ)	0.05	−0.007	0.000	−0.01	0.001	−0.04	0.002	0.14	0.007	0.09	0.005	−0.06	0.003	−0.03	0.002
Color variance (σ_c)	0.03	0.03	0.001	0.52	0.016	−0.173	0.005	0.53	0.016	...	0.100	...	0.011	...	0.004
Total			0.088		0.091		0.092		0.270		0.097		0.012		0.014

the two parameterizations:

$$q_0 = \tfrac{1}{2}\left(\Omega_m + \Omega_{DE}\left(1 + 3w\right)\right),$$
$$j_0 = \Omega_m + \frac{\Omega_{DE}}{2}\left(2 + 9w\left(1 + w\right)\right), \qquad (8)$$
$$\Omega_k = \Omega_m + \Omega_{DE} - 1.$$

In Figure 19, we show the sum of the jerk and curvature ($j + \Omega_k$) as a function of q_0. A constant value of the jerk is assumed. The gray shading indicates the region where the luminosity distance expansion is valid.[29] The blue contours represent the CSP data using the Caldwell & Kamionkowski (2004) parameterization. The black contours, representing the baryon acoustic oscillation data, were generated using the transformation equations above. The joint constraints from the CSP and baryon acoustic oscillation data yield a value of $j_k = 1.18 \pm 0.44$ (statistical) ± 0.27 (systematic) and $q_o = -0.67 \pm 0.13$ (statistical) ± 0.09 (systematic) at the 95% confidence level. Since jerk and curvature are combined, no assumption of flatness is required. We note that to within the uncertainties, these parameters are consistent with the standard dynamical model with $w = -1$. With future, larger data sets, the discrimination among competing models will be sharpened and this type of kinematical prescription will offer a valuable independent test of the current standard cosmology.

9.3. Systematic Uncertainties

To quantify the effects of systematic errors, we model the effects of known and potential systematic errors for each of the five cosmological parameters discussed in this paper (w, Ω_m, Ω_{DE}, q_0, and j_0). We present in Table 8 the main sources of uncertainty that could contribute to a systematic error, including magnitude and color offsets between the low- and high-redshift samples, errors in the color terms used to transform the instrumental magnitudes to our natural system, and biases due to the method of χ^2-minimization. We have aimed to give a conservative estimate of the uncertainties. The first column describes the potential source of error and the second column provides a bound on its magnitude. For each of the cosmological parameters, we tabulate the rate of change of the parameter with respect to the systematic (Columns 3, 5, 7, 9, 11, 13, and 15) and the resulting error on the parameter (Columns 4, 6, 8, 10, 12, 14, and 16). The main sources of potential systematic errors and how we simulate their effects are discussed in more detail in the Appendix.

The final systematic errors adopted are obtained by summing in quadrature the contributions listed in Table 8. From this table, we can see that the current systematic total uncertainty in our

---

[29] Specifically, the error incurred by not including the fourth order term in the Taylor series expansion results in a distance modulus error of ± 0.3 mag at a redshift of 0.7.
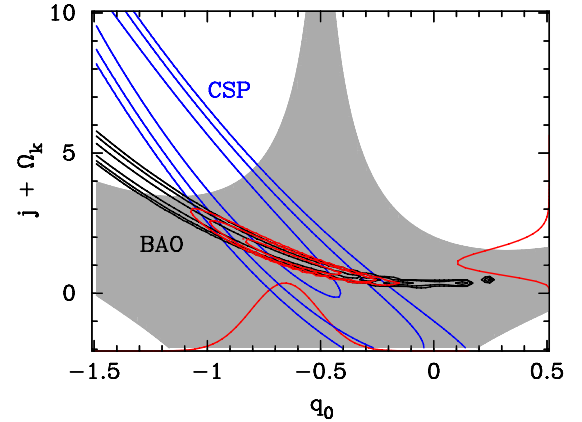
Figure 19. Sum (j_k) of the jerk (j) and curvature parameter (Ω_k) as a function of the deceleration parameter (q_0). The gray shading indicates the region where the luminosity distance expansion is valid, as described in the text. The best-fit values including both baryon acoustic oscillation and the CSP data are $j_k = 1.18 \pm 0.44$ (statistical) ± 0.27 (systematic) and $q_o = -0.67 \pm 0.13$ (statistical) ± 0.09 (systematic) at the 95% confidence level. The one-dimensional marginalized probabilities for each parameter are plotted as red lines on the axes.

(A color version of this figure is available in the online journal.)

measurement of w is $\pm 9\%$. A key element for future SNe Ia studies is improving the absolute calibration of photometric standards (particularly in the era of the Joint Dark Energy Mission, JDEM), ensuring that the calibration minimizes color uncertainties as optical and NIR measurements are compared. Decreasing the uncertainty due to reddening is another critical component of minimizing the overall systematic errors.

Finally, we summarize in Table 9 the values of cosmological parameters from this paper calculated under different sets of assumptions, as described in Section 9.1, along with both their statistical and systematic uncertainties. When the analysis of our total sample of 75 high-redshift SNe Ia is complete, our statistical and systematic uncertainties will be comparable.

10. SUMMARY AND FUTURE MEASUREMENTS

We have used ground-based NIR measurements of SNe Ia to yield an independent Hubble diagram based on *rest-frame i*-band data. Reddening effects are a priori lower in the red than the ultraviolet–blue–visual, and we find that *i*-band photometry is an effective tool for minimizing systematic effects for SNe Ia. Our new observations of 21 SNe Ia at $0.01 < z < 0.08$ and 35 SNe Ia at $0.12 < z < 0.70$, yield the following results.

1. These first CSP data provide independent evidence for an accelerating universe. In the context of a cosmological model including a component of dark energy, $\Omega_{DE} > 0$ at significantly greater than the 99% confidence level.

Table 9
Summary of Cosmological Parameters

Constraints	Cosmological Parameters
$w = -1$	$\Omega_m = 0.27 \pm 0.02$ (statistical)
Combine with BAO	$\Omega_{DE} = 0.76 \pm 0.13$ (statistical) ± 0.09 (systematic)
$\Omega_k = 0$	$\Omega_m = 0.27 \pm 0.03$ (statistical)
Combine with BAO	$w = -1.05 \pm 0.13$ (statistical) ± 0.09 (systematic)
Constant j	$q_o = -0.67 \pm 0.13$ (statistical) ± 0.09 (systematic)
Combine with BAO	$j_k = 1.18 \pm 0.44$ (statistical) ± 0.27 (systematic)

2. Joint SN Ia plus baryon acoustic oscillation constraints yield $w = -1.05 \pm 0.13$ (statistical) ± 0.09 (systematic) and $\Omega_m = 0.27 \pm 0.03$ (statistical). When the analysis of our total sample of 75 high-redshift SNe Ia is complete, our statistical and systematic uncertainties will be comparable, and at the $\pm 10\%$ level.

3. A purely kinematic solution, with no assumptions about the matter and energy content of the universe, yields values of $j_k = 1.18 \pm 0.44$ (statistical) ± 0.27 (systematic) and $q_o = -0.67 \pm 0.13$ (statistical) ± 0.09 (systematic) for the cosmic jerk and the deceleration parameter, respectively. These results are consistent with an acceleration of the expansion of the universe, and with the current standard model of cosmology.

4. The current sample of SN Ia photometry is inconsistent with the application of a standard Milky Way reddening law alone, suggesting either that intrinsic color effects dominate the standard reddening corrections, that the SNe Ia are being reddened by dust with different properties than that in the Milky Way, or perhaps there is circumstellar dust about the SN Ia. Future SNe Ia studies will need to disentangle these effect to decrease the systematic errors for SN Ia cosmology.

Beyond a redshift of 0.7, the i band (at rest frame 7600 Å) is shifted beyond the 1.2 μm J band in the NIR, rendering i band measurements impossible from the ground. Even before this limit is reached, observations from space are desirable in order to eliminate the bright terrestrial sky background. The CSP data quantitatively illustrate the utility of longer wavelength data in minimizing systematic uncertainties for SNe Ia cosmology, of relevance for future planned space missions such as the NASA/DOE JDEM. We suggest that a combination of ground, HST, and future space observations are needed to measure accurately the i-band Hubble diagram and constrain the values of w and w_a to the highest possible accuracy.

Finally, we note that while SNe Ia currently provide the most compelling evidence for the acceleration of the universe, ultimately a combination of different techniques will be required to measure not only w, but also its time evolution. Existing degeneracies are such that accurate constraints can be obtained only in the combination of several techniques, or explicitly making the assumption that the universe is flat ($\Omega_{TOT} = 1$). Future studies of baryon acoustic oscillations, weak lensing, clusters of galaxies, and SNe Ia will yield further complementary and independent estimates of w and w_a. SNe Ia will remain a valuable component of future investigations because they naturally cover the redshift range (0.1–0.6) where dark energy is measured to be dominant, and cosmic variance is not a major issue for them.

APPENDIX

SYSTEMATIC ERROR BUDGET

In this appendix, we outline our method for estimating the effects of systematic errors in the determination of various parameters. We have categorized the various sources of error based on their functional form. We then compute the sensitivity of the cosmological parameters to these functions through simulations. Finally, we compute the magnitude of each effect by summing the systematics for each category in quadrature. Table 8 summarizes the sensitivity of each parameter to each systematic. We also illustrate the effects of these systematic effects on the calculated parameters in graphical form.

A.1. Magnitude Offset Between Low and High z

The low- and high-z observations are obtained on different telescopes, and therefore are calibrated independently, which can potentially introduce a simple magnitude offset between the zero points of the low- and high-z data. We model this effect by simply adding fixed values, δ_m, to the high-z peak magnitudes and recompute the best-fit cosmology.

The results of this simulation are shown in Figure 20 and show that to a good approximation, the systematic effect of a magnitude offset on w is a linear function of δ_m with slope $dw/d\delta_m = -2.69$ in the i band and $dw/d\delta_m = -2.66$ in the B band. Furthermore, there is no significant effect on the three nuisance parameters.

To estimate the value of δ_m, we consider the following possible sources of such an offset: (1) error in the Y and J zero points, (2) error in the i-band zero point, and (3) errors in the extinction coefficients. We describe each in turn.

The contribution to the systematic uncertainty in δ_m has a different origin for the Y and J filters. As described in Section 4.4, we have used Kurucz models to extend the energy distributions of the Persson et al. (1998) standards from J (1.25μ) to Y (1.035μ) (Hamuy et al. 2006). That this was viable was confirmed by Contreras et al. (2009), who showed that the zero-color A0 star Feige 16 does in fact have $Y - J = -0.009 \pm 0.016$, confirming this calibration to an accuracy of ± 0.01 mag. Conservatively, we adopt an error in the zero point for the Y band of ± 0.025.

In the case of J, the main problem is the changing amount of water vapor above the telescope. An increase manifests itself as a systematic narrowing of the passband. This may or may not show up in standard star measurements, depending on when
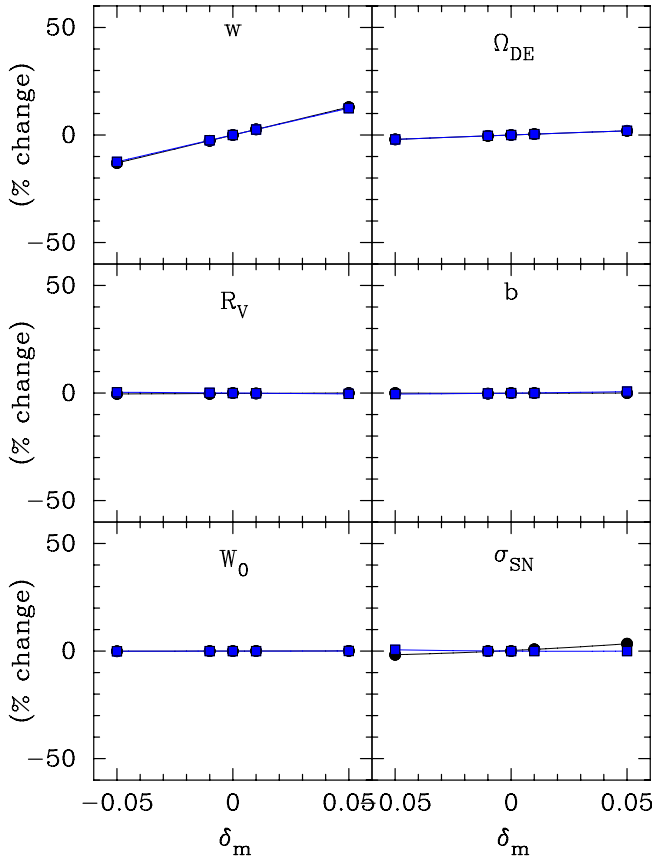
Figure 20. Effect of a magnitude offset δ_m on the best-fit parameters w, Ω_{DE}, R_V, B, W_0, and σ_{SN}. The black circles are for i band, while the red squares are for B band. In almost all cases, the differences in the points are negligible. The lines are quadratic fits. The largest sensitivity to a magnitude offset is for w. For an offset of 0.025 magnitudes, the percentage change in w amounts to 7%.
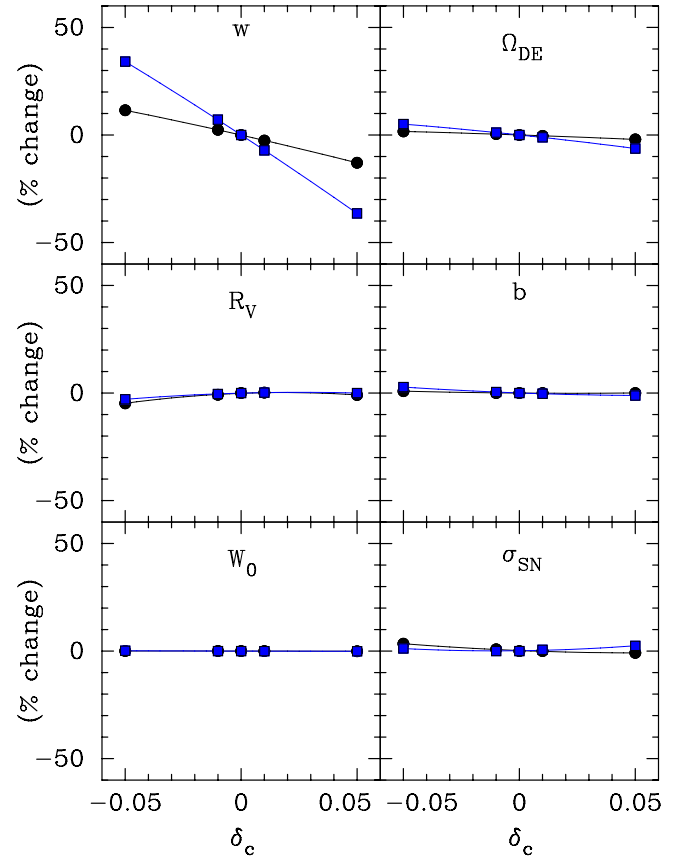
(A color version of this figure is available in the online journal.)

Figure 21. Effect of a color offset δ_c on the best-fit parameters, as listed in Figure 20. The black circles are for i band, while the red squares are for B band. The lines are quadratic fits. The largest sensitivity to a color offset is again for w. For a color offset of 0.02 mag, the percentage change in w amounts to 5%.

(A color version of this figure is available in the online journal.)

during the night they were measured. We adopt an error in the zero point for J band of ± 0.015.

The common ancestor to the Persson et al. (1998) and Smith et al. (2002) systems is Vega. We, therefore, must determine the zero point of the i band relative to Vega instead of BD $+17°4708$ in order to compute consistent zero points. We have investigated the effects of a systematic error in the SED of Vega by comparing synthetic i-band photometry using the Bohlin (2007) and Bohlin & Gilliland (2004) SEDs. The difference is 0.01 mag. We further investigated uncertainties in our i-band filter transmission function. In constructing all our CSP filters, shifts in wavelength needed to be applied in order to have the synthetic color terms match the observed color terms (Contreras et al. 2009). A typical uncertainty in these shifts is approximately 10 Å, which is equivalent to an error of ± 0.001 mag. We, therefore, estimate a zero-point error of ± 0.01 for the i band.

According to Hamuy et al. (2006) and Contreras et al. (2009), the dispersion in the extinction coefficient for the i band is ± 0.03. The median airmass of our SNe Ia observations in the i band was 1.315, and so we estimate a systematic error of ± 0.009 mag due to dispersion in the extinction coefficient. Similar errors are expected for the Y- and J-band filters, though the median airmass for our high-redshift observations is typically lower (1.24). We, therefore, estimate a total error of ± 0.01 mag.

Given the external check with the standard star Feige 16 (Contreras et al. 2009), we believe our calibration to be robust.

Nevertheless, we allow for a conservative systematic magnitude offset between low- and high redshift of $\delta_m = \pm 0.025$ mag.

A.2. Color Offset Between Low and High z

This systematic is analogous to the magnitude offset and can occur for the same reasons; however, it propagates through the analysis differently as it is multiplied by the reddening coefficient. We proceed in the same manner as before, adding a color offset δ_c to the $(B - V)$ colors at high z and compute the best-fit cosmology. As in the previous case, the effect on the cosmological parameters is linear (see Figure 21). However, the effect on the B band is more than twice that in the i band ($dw/d\delta_c = 2.53$ and $dw/d\delta_c = 7.53$, respectively). This is simply due to the fact that the reddening coefficient is twice as large at B relative to the i band. An advantage is that the colors we use in our analysis are all constructed from the same optical photometric systems and avoid the NIR and the i band. We estimate the total possible color offset to be $\delta_c = \pm 0.02$.

A.3. Estimation of Uncertainties

The method of χ^2-minimization suffers from a well-known bias when there is measurement error in the independent variables (Kelly 2007). The root of the problem lies in the fact that the numerator of χ^2 (see Equation (4)) is sensitive to the model parameters only, whereas the denominator is sensitive to the nuisance parameters as well as the variances (see Equation (5)). As such, the best-fit solution is a function
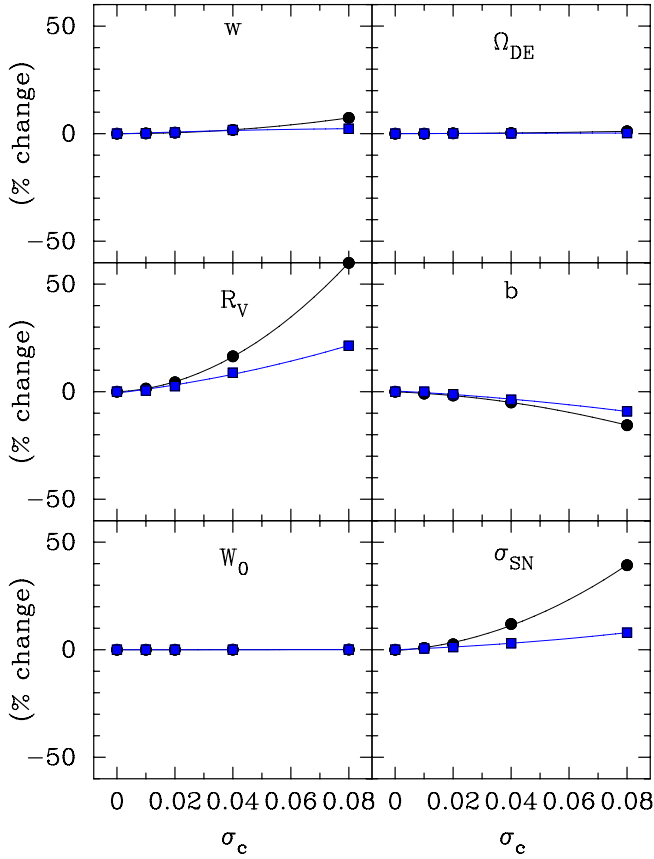
Figure 22. Effect of extra variance in the color measurements σ_c on the best-fit parameters, as listed in Figure 20. The black circles are for i band, while the red squares are for B band. The lines are quadratic fits. A variance in the color measurements impacts the determination of the reddening law or color term. A variance of ± 0.03 magnitudes results in a percentage change in R_V of 10%. The impact on cosmology is very small.

(A color version of this figure is available in the online journal.)
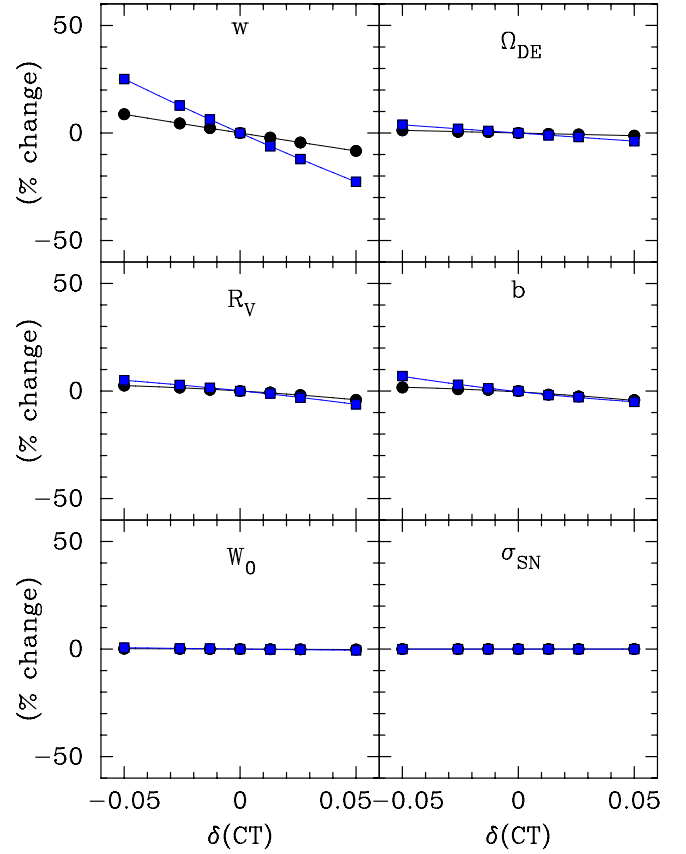
Figure 23. Effect of an error in the color term derived from local sequences of standards, as listed in Figure 20. The black circles are for i band, while the red squares are for B band. The lines are quadratic fits. An error in the color term has the largest impact on w. For an error of 0.015, the percentage change in w amounts to 3%.

(A color version of this figure is available in the online journal.)

not only of the data, but also the variances, complicating the computation of the overall systematic uncertainties.

We have investigated the effect of adding extra variance to both the colors σ_c^2 and Δm_{15}. Figure 22 shows the strong dependence of R_V on σ_c. The i-band data are about a factor of 2, less sensitive to changes in R_V than the B-band data. As a result, the bias due to the denominator of χ^2 is larger in the i band. If we were to include more heavily reddened objects (for instance, SN 2005A and SN 2006X), then this effect would disappear entirely. The effects of extra variance in Δm_{15} are not significant and are therefore not shown, though they are included in Table 8 for completeness.

A.4. Color Gradient

Color terms are used to transform the magnitudes of the standard stars to the natural CSP system. These color terms are empirically determined and therefore suffer from measurement uncertainty. An error in the color terms could potentially introduce a color gradient in the data: color errors that correlate with the instrumental color of the SNe Ia. Figure 23 shows the sensitivity functions. As expected, the impact in the B band is larger than in the i band. From Hamuy et al. (2006) and Contreras et al. (2009), we estimate $\delta(\mathrm{CT}) = 0.015$, which is the typical 1σ error in the color terms.

REFERENCES

Alard, C. 2000, A&AS, 144, 363
Alard, C., & Lupton, R. H. 1998, ApJ, 503, 325
Albrecht, A., et al. 2006, DETF Report (arXiv:astro-ph/0609591)
Astier, P., et al. 2006, A&A, 447, 31
Balland, C., et al. 2006, A&A, 445, 387
Bertin, E., & Arnouts, S. 1996, A&AS, 117, 393
Blandford, R. D. 2004, in Measuring and Modeling the Universe, ed. W. L. Freedman (Carnegie Observatories Astrophysics Series; Cambridge: Cambridge Univ. Press), 377
Blondin, S., et al. 2006, AJ, 131, 1648
Bohlin, R. C. 2007, in ASP Conf. Ser. 364, The Future of Photometric, Spectrophotometric, and Polarimetric Standardization, ed. C. Sterken (San Francisco, CA: ASP), 315
Bohlin, R. C., & Gilliland, R. L. 2004, AJ, 127, 3508
Caldwell, R. R., & Kamionkowski, M. 2004, J. Cosmol. Astropart. Phys., JCAP09(2004)009
Cardelli, J. A., Clayton, G. C., & Mathis, J. S. 1989, ApJ, 345, 245
Conley, A., et al. 2008, ApJ, 681, 482
Contreras, C., et al. 2009, AJ, in press
Draine, B. T. 2003, ARA&A, 41, 241
Eisenstein, D. J., et al. 2005, ApJ, 633, 560
Elias, J. H., Frogel, J. A., Matthews, K., & Neugebauer, G. 1982, AJ, 87, 1029
Elias, J. H., Matthews, K., Neugebauer, G., & Persson, S. E. 1985, ApJ, 296, 379
Ellis, R. S., et al. 2008, ApJ, 674, 51
Folatelli, G., et al. 2006, ApJ, 641, 1039
Folatelli, G., et al. 2009, AJ, in press
Foley, R. J., et al. 2008, ApJ, 684, 68
Freedman, W. L., et al. 2001, ApJ, 553, 47

Frieman, J. A., Turner, M. S., & Huterer, D. 2008, ARA&A, 46, 385
Frieman, J. A., et al. 2008, AJ, 135, 338
Gallagher, J. S., Garnavich, P. M., Caldwell, N., Kirshner, R. P., Jha, S. W., Li, W., Ganeshalingham, M., & Filippenko, A. V. 2008, ApJ, 685, 752
Goobar, A. 2008, ApJ, 686, L103
Hamuy, M., Phillips, M. M., Maza, J., Suntzeff, N. B., Schommer, R. A., & Aviles, R. 1995, AJ, 109, 1
Hamuy, M., Phillips, M. M., Suntzeff, N. B., Schommer, R. A., Maza, J., & Aviles, R. 1996a, AJ, 112, 2398
Hamuy, M., Phillips, M. M., Suntzeff, N. B., Schommer, R. A., Maza, J., & Aviles, R. 1996b, AJ, 112, 2391
Hamuy, M., Phillips, M. M., Suntzeff, N. B., Schommer, R. A., Maza, J., Smith, R. C., Lira, P., & Aviles, R. 1996c, AJ, 112, 2438
Hamuy, M., Trager, S. C., Pinto, P. A., Phillips, M. M., Schommer, R. A., Ivanov, V., & Suntzeff, N. B. 2000, AJ, 120, 1479
Hamuy, M., et al 2006, PASP, 118, 2
Hawkins, E., et al. 2003, MNRAS, 346, 78
Hicken, M., Wood-Vasey, W. M., Blondin, S., Challis, P., Jha, S., Kelly, P. L., Rest, A., & Kirshner, R. P. 2009, ApJ, 700, 1097
Hillenbrand, L. A., Foster, J. B., Persson, S. E., & Matthews, K. 2002, PASP, 114, 708
Holtzman, J. A., et al. 2008, AJ, 136, 2306
Holz, D. E. 1998, ApJ, 506, L1
Hook, I. M., et al. 2005, AJ, 130, 2788
Hsiao, E. Y., Conley, A., Howell, D. A., Sullivan, M., Pritchet, C. J., Carlberg, R. G., Nugent, P. E., & Phillips, M. M. 2007, ApJ, 663, 1187
Jha, S., Riess, A. G., & Kirshner, R. P. 2007, ApJ, 659, 122
Kasen, D. 2006, ApJ, 649, 939
Kelly, B. C. 2007, ApJ, 665, 1489
Kim, A., Goobar, A., & Perlmutter, S. 1996, PASP, 108, 190
Knop, R. A., et al. 2003, ApJ, 598, 102
Krauss, L. M., & Chaboyer, B. 2003, Science, 299, 65
Krisciunas, K., et al. 2001, AJ, 122, 1616
Landolt, A. U. 1992, AJ, 104, 340
Linder, E. V. 2006, Astropart. Phys., 26, 102
Lira, P. 1995, Master's thesis, Univ. Chile
Madore, B. F. 1982, ApJ, 253, 575

Martini, P., Persson, S. E., Murphy, D. C., Birk, C., Shectman, S. A., Gunnels, S. M., & Koch, E. 2004, Proc. SPIE, 5492, 1653
Matheson, T., et al. 2005, AJ, 129, 2352
Meikle, W. P. S. 2000, MNRAS, 314, 782
Miknaitis, G., et al. 2007, ApJ, 666, 674
Naylor, T. 1996, MNRAS, 296, 339
Nobili, S., & Goobar, A. 2008, A&A, 487, 19
Nobili, S., et al. 2005, A&A, 437, 789
Nugent, P., Kim, A., & Perlmutter, S. 2002, PASP, 114, 803
Perlmutter, S., et al 1999, ApJ, 517, 565
Persson, S. E., Murphy, D. C., Krzeminski, W., Roth, M., & Rieke, M. J. 1998, AJ, 116, 2475
Phillips, M. M. 1993, ApJ, 413, L105
Phillips, M. M., Lira, P., Suntzeff, N. B., Schommer, R. A., Hamuy, M., & Maza, J. 1999, AJ, 118, 1766
Phillips, M. M., et al. 2007, PASP, 119, 360
Pinto, P. A., & Eastman, R. G. 2000, ApJ, 530, 757
Prieto, J. L., Rest, A., & Suntzeff, N. B. 2006, ApJ, 647, 501
Riess, A. G., Press, W. H., & Kirshner, R. P. 1996, ApJ, 473, 88
Riess, A. G., et al. 1998, AJ, 116, 1009
Riess, A. G., et al. 2000, ApJ, 536, 62
Riess, A. G., et al. 2004, ApJ, 607, 665
Riess, A. G., et al. 2007, ApJ, 659, 98
Sako, M., et al. 2008, AJ, 135, 348
Schlegel, D. J., Finkbeiner, D. P., & Davis, M. 1998, ApJ, 500, 525
Smith, J. A., et al. 2002, AJ, 123, 2121
Spergel, D. N., et al. 2003, ApJS, 148, 175
Spergel, D. N., et al. 2007, ApJS, 170, 377
Stetson, P. B. 1990, PASP, 102, 932
Sullivan, M., et al. 2003, MNRAS, 340, 1057
Tremaine, S., et al. 2002, ApJ, 574, 740
Tripp, R. 1998, A&A, 331, 815
Tripp, R., & Branch, D. 1999, ApJ, 525, 209
Wang, L., Strovink, M., Conley, A., Goldhaber, G., Kowalski, M., Perlmutter, S., & Siegrist, J. 2006, ApJ, 641, 50
Wood-Vasey, W. M., et al. 2007, ApJ, 666, 694
York, D. G., et al. 2000, AJ, 120, 1579